ABSTRACT

Title of Dissertation: DYNAMICS AND CONTROL
OF BIOINSPIRED SWIMMING,
SCHOOLING, AND PURSUIT

Anthony Thompson
Doctor of Philosophy, 2023

Dissertation Directed by: Professor Derek Paley
Department of Aerospace Engineering

Understanding the benefits of the behaviors of aquatic animals can improve the capabilities of robotic systems. Aquatic species such as the zebrafish swim with discrete motions that alternate between perception and action while avoiding predators and swimming in schools, and other species such as the lionfish use their pectoral fins to herd and trap prey. This work seeks to model these bioinspired behaviors (i.e., schooling, swimming with intermittent sensing and actuation, and pursuit and evasion in a structured environment) and enhance our understanding of their benefits.

A hybrid dynamic model is derived with two phases; namely a burst phase during which each particle applies a control input and a coast phase during which each particle performs state estimation. This model provides a way to investigate how having non-overlapping sensing and control affects a multi-agent system's ability to achieve collective behavior such as steering to some desired direction. By evaluating the stability properties

of the equilibrium points for the collective behavior, investigators can determine parameter values that exhibit exponentially stable behavior.

Aside from swimming intermittently, fish also need to avoid predators. Inspired by observations of predation attempts by lionfish (*Pterois sp.*), a pursuit-evasion game is derived in a bounded environment to study the interaction of an advanced predator and an intermittently steering prey. The predator tracks the prey with a pure-pursuit strategy while using a bioinspired tactic to minimize the evader's escape routes, i.e, to trap the prey. Specifically, the predator employs symmetric appendages inspired by the large pectoral fins of lionfish, but this expansion increases its drag. The prey employs a bioinspired randomly-directed escape strategy to avoid capture and collisions with the boundary known as the protean strategy. This game investigates the predator's trade-off of minimizing the work to capture the prey and minimizing the prey's escape routes. Using the predator's expected work to capture as a cost function determines when the predator should expand its appendages as a function of the relative distance to the evader and the evader's proximity to the boundary.

Prey fish also swim in schools to protect themselves from predators. To drive a school of fish robots into a parallel formation, a nonlinear steering controller is derived and implemented on a robotic fish platform. These robotic fish are actuated with an internal reaction wheel driven by a DC motor. Implementation of the proposed parallel formation control law on an actual school of soft robotic fish is described, including system identification experiments to identify motor dynamics and the design of a motor torque-tracking controller to follow the formation torque control. Experimental results demonstrate a school of four robotic fish achieving parallel formations starting from random initial conditions.

Dynamics and Control of Bioinspired Swimming, Schooling, and Pursuit

by

Anthony Allan Thompson

Dissertation submitted to the Faculty of the Graduate School of the
University of Maryland, College Park in partial fulfillment
of the requirements for the degree of
Doctor of Philosophy
2023

Advisory Committee:
      Professor Derek Paley, Chair/Advisor
      Professor Hugh Bruck, Dean's Representative
      Professor Yancy Diaz-Mercado
      Professor Micheal Otte
      Professor Eleonora Tubaldi
      Professor Dave Akin

Dedication

I dedicate this dissertation to my wife Vashti, my daughter Lena, and friend Juwan Howard.

Acknowledgments

I want to thank my advisor Dr. Derek Paley for giving me the opportunity to pursue a Ph.D in aerospace engineering and teaching me a variety of topics pertaining to dynamics and control theory. He helped me grow as a researcher and taught me how to present my research in a meaningful and digestible manner for a diverse audience. Dr. Paley encouraged me to expand my interest beyond building robotic systems and performing experiments, and he taught me the importance of a theoretical understanding of engineered systems.

I also want to thank my dissertation committee for their time, their feedback for the work presented in this dissertation, and the lessons that they have taught me over the years. A special thanks goes to Dr. Diaz-Mercado, Dr. Otte, and Dr. Tubaldi, for expanding my knowledge in control theory, networked systems, path planning, and fluid structure interactions. They topics make me a well-rounded engineer.

Additional acknowledgement and thanks goes to Dr. Matt McHenry and Dr. Ashley Peterson at the University of California, Irvine for collaborating on research, providing an understand of biological behaviors and capabilities for many fish species, and inspiring me to better utilize graphics to tell a story when presenting my research.

Lastly, I would like to acknowledge financial support from the Office of Naval Research (ONR) and the Maryland Robotics Center (MRC) for all of the projects discussed herein.

Table of Contents

List of Tables

List of Figures

Chapter 1:   Introduction

Stemming back from the philosophy of Darwinism, a common belief in many scientific disciplines is that biological systems tend to naturally optimize themselves over time. We as engineers often draw inspiration from biology to enhance our knowledge and ability to develop pre-optimized engineered systems.

For example, biological species ranging from gray squirrels to zebrafish traverse their environments with discrete motions that alternate between perception and action [1–6]. For underwater species, like the zebrafish and rummy-nose tetra, this discrete behavior is hypothesized to be the result of the perceptual degradation in their sensory organs due to self-generated motions like swimming [6–8]. In fact, some zebrafish desensitize their lateral line system, a sensory organ system used to measure the pressure gradient of the surrounding fluid, during active swimming [7]. For fish, these intermittent swimming behaviors offer many benefits including reduced cost of transport, enhanced functionality of sensory organs, improved localization in pursuit of prey, and ample time to process the perceived environment and formulate motor commands in response [1,5,7].

While much attention has been given to modeling a fish's swimming kinematics, little attention has been given to the idea that some fish species have active swimming periods where they are sensory deprived and non-active periods where they are sensory rich. What

happens to an engineered system when there is non-overlapping sensing and control? Here we devise a hybrid model of intermittent locomotion with non-overlapping sensing and control. With this model we're able to draw conceptual and technical conclusions of how the stability changes due to intermittent locomotion.

While there are benefits to having intermittent locomotion, biological fish do more than just swim. Fish also need to hunt and avoid predators. While observing the pursuit interactions between a lionfish and its intermittently swimming prey, biologist have noted that lionfish tend to spread their pectoral fish in an effort to herd prey [9, 10]. Lionfish tend to also reside near coral reefs where the structures in the environment may play a role in predation. While this herding behavior may seem intuitive and quite trivial, spreading the pectoral fins increases the lionfish's frontal surface area and therefore increases its drag. It is unclear, why this predator would choose work harder to catch prey, and it is unclear if the structures in the environment affect the lionfish's pursuit tactics. In this dissertation we use differential game theory to create a pursuit-evasion game with a single predator and a single prey in a bounded environment, inspired by observations of predation attempts by lionfish (*Pterois sp.*). The model for this game allows researchers to study the trade-off between minimizing the predator's work to capture the prey and minimizing the prey escape routes by expanding its pectoral fins. This model also sheds light on how boundaries in the environment can be beneficial to predators.

1.1 Relation to Prior Work

The work in this dissertation builds on similar work done by others. In this section, I highlight the relation of this work to prior work, and I describe how this work pushes the envelope further. First, I discuss prior work for hybrid models with intermittent locomotion. Second, I highlight biological observations of predator-prey interactions for lionfish, and I study this type of interaction with a differential game. Third, I discuss prior work on formation control for underwater vehicles.

1.1.1 Intermittent Sensing and Actuation

While the kinematic modeling of intermittent swimming in biological fish has received ample attention, the dynamic modeling of these behaviors in fish is not well studied. The works in [11–13] model the viscous drag forces on the body of a fish and investigate the energy saving benefits of intermittent swimming as compared to continuous swimming. Intermittent swimming is found to be more energy efficient than continuous swimming at high Reynolds numbers and with moderate values for the duty cycle between the burst and coast phases [12, 13]. Other research in this area neglects the effects of viscous drag and uses a variation of Vicsek's particle model [14], to describe the dynamics of multiple self-propelled particles while focusing on intermittent consensus control.

In [15–18], multi-agent intermittent consensus controllers were derived for agents with self-propelled particles dynamics with both synchronous and asynchronous updates. For the synchronous intermittent consensus controllers, the agents share and update their states at equivalent discrete times, whereas for the asynchronous controllers the agents

have delays between their discrete updates. The intermittency of the state-feedback controllers were dictated by event-triggered protocols for the control inputs [15,16] and switched communication topologies [17]. The main result from these works is that the stability conditions of the asynchronous consensus controllers are similar to that of the synchronous controllers, but also depend on the difference in discrete time updates. For intermittent consensus problems, the agents have Euclidean dynamics and rendezvous to a single point. However, in our work we are interesting in the intermittent heading synchronization observed in schooling fish.

Multi-particle synchronization on the N-torus using state-feedback controllers is well studied [14, 19–23]. In [22], a discrete-time state-feedback controller synchronizes the headings of multiple self-propelled particles with asynchronous updates. The key assumptions in [22] are as follows: the particles share their orientation on a fixed communication graph, every particle is updated over a uniform time horizon, and only disconnected particles update at the same time. Under these assumptions, any locally asynchronous descent algorithm is shown to drive the particles to synchronize there headings. The work presented here relaxes some of these assumptions and extends these results to controllers with output feedback, where each particle estimates the relative headings of its neighbors.

Much of the research on intermittent consensus and synchronization relies on the assumption that each agent knows the relative states of its neighbors. In contrast, [24] uses output feedback control laws on multiple second order self-propelled particles to drive them into parallel and circular formations. The multi-particle system has a fixed communication graph and each particle estimates the relative velocity of its neighbors with the knowledge of their relative distances and turning rates. Lyapunov's direct method was

used to prove that the errors in estimated relative velocity are ultimately bounded and the desired equilibrium points were practically stable.

1.1.2 Bioinspired Pursuit in a Structured Environment

Interactions between predators and their prey have fascinated a variety of scientific disciplines for several decades. For biologists, predator-prey interactions inform the structure of ecosystems [25–27], and characterize the pursuit behavior of predators [1, 9, 10, 25, 28–30], and the evasive behavior of prey [31–34]. Engineers and mathematicians use these interactions to develop dynamic and kinematic models for missile guidance [35], differential games [36, 37], and to derive pursuit and evasion strategies for robotic systems [38–45].

Pursuit-evader games attempt to derive optimal pursuit strategies by modeling both agents as particles. These particle models are often based on the kinematic modeling from [35] and used in the theoretical differential games from [36]. In [35], Shneydor derives kinematic models for missiles guidance for a variety of pursuit strategies like classical pursuit, known as pure-pursuit, deviated pure-pursuit, and parallel navigation, also known as motion camouflage. Differential games consider the kinematics of both agents and study how their pursuit and evasion strategies affect the outcome of the interaction. For zero-sum differential games, the pursuer seeks to minimize some cost function and the evader seeks to maximize it such that the total sum of their costs is zero [36]. A common assumption of kinematic pursuit models is that the pursuer is faster than the evader which guarantees that the evader is captured [35, 38, 42]. However, capture of a faster evader is

possible for a slower pursuer by using the Apollonius circle pursuit method. A slow pursuer computes the points of intersection between its Appolonius circle and the evader's trajectory; where the circle's center and radius corresponds to the positions where capture is guaranteed [41, 45, 46]. This model assumes pursuit of a faster non-maneuvering evader, while [35] assumes the evader is non-maneuvering and is slower than the pursuer. These mathematical frameworks give insight about the pursuit trajectories and provide conditions on both the pursuer and the evader for capture and evasion. With these conditions as a foundation, a kinematic model can be used to determine the time required to capture the evader.

The unique ability of animals to alter their behavior, locomotion, and morphology in response to a stimuli inspires and informs both biologists and engineers. Fishes are widely studied by engineers interested in developing control systems and autonomous underwater vehicles. Bioinspiration also plays an integral role in pursuit-evasion games [37, 38] and pursuit-evasion models have previously been applied to a handful of fish species [1, 30, 31, 34, 42]. For example, lionfish (*Pterois sp.*) will actively pursue maneuverable prey fishes with a pure-pursuit targeting strategy, often approaching their target slowly to avoid inducing a startle response [27, 28, 31]. In addition, lionfish have large fan-like pectoral fins (depicted in Figure 1.1(a-b)) that may serve to restrict prey movement [9, 10]. The large surface area of the pectoral fins are likely drag inducing, yet lionfish rarely pursue a prey without expanding them. To understand the benefits of employing these large appendages we test their effect on a pursuit-evasion game. In this game the pursuer is modeled as a rigid streamlined body with symmetric appendages in pure-pursuit of the evader. In the resting orientation, the pursuer's appendages are held against the body, parallel to the

pursuer's sagittal plane as in Figure 1.1(c), while in the active orientation the appendages are expanded perpendicular to the sagittal plane as in Figure 1.1(d). The pursuer uses its appendages to minimize the evader's escape routes, but this orientation increases the pursuer's surface area and therefore its drag.

(a) Lionfish (*Pterois sp.*)

(b) Lateral view

(c) Model of pursuer with symmetric appendages

(d) Pursuer's appendages in an active orientation
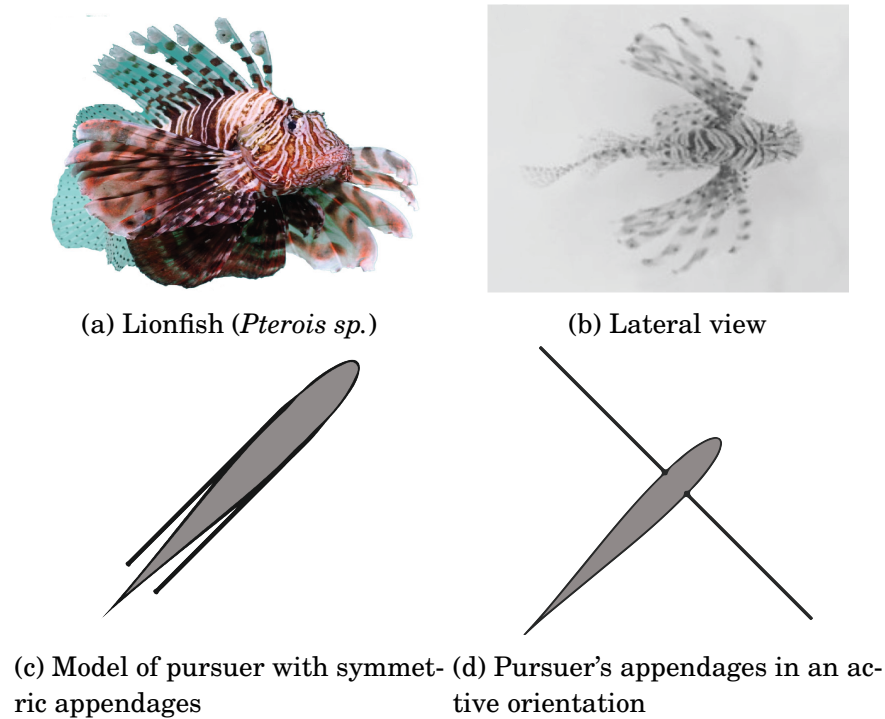
Figure 1.1: Lionfish (*Pterois sp.*) serve as bioinspiration for a shape changing predator. (a) Lateral view of a lionfish (*Pterois miles*) (b) Dorsal view of a lionfish (*Pterois volitans*; in black and white); (c) depicts the model of the pursuer with appendages in the resting orientation; and (d) the pursuer's appendages are in an active orientation.

In biological systems animal prey may employ an optimal evasion strategy (classical evasion), where the evader attempts to maximize the relative distance to the pursuer [31, 34, 47] or a protean strategy, where the evader senses the relative position of the pursuer and flees in a random direction to be less predictable [31–33, 48]. Observations of an evader's escape direction yields a probability density function that is used for mathematical predictions [33]. The movement patterns of animals also play a role in the pursuit-

evasion interaction. Mathematical models often assume constant locomotion, however, a variety of aquatic, aerial, and terrestrial species use intermittent locomotion [2, 3]. For many fishes this intermittent locomotion is split into two discrete phases that correspond with acceleration and deceleration. During the acceleration phase the fish will generate thrust and actively steer itself, while during the deceleration phase the fish glides through the water without active steering [1, 7]. Inspired by the intermittent prey from the observations in [28, 29], the evader in the present study uses an intermittent-steering kinematic model (with a constant speed) and a protean evasion strategy to evade the pursuer and to avoid collisions with the boundary.

1.1.3   Formation Control for Multiple Robotic Fish

Collective behavior of mobile agents has received significant interest recently in fields such as biology, physics, computer science, and control engineering [49–51]. Research in this area is allowing scientists to better understand swarming behavior in nature and benefits control engineers in numerous applications by mimicking nature's behavior in engineered mobile systems such as unmanned ground, air, and underwater vehicles.

Previous investigations of bioinspired underwater vehicles include the design, sensing, and control of a single fish-inspired robot that is driven by an internal reaction wheel [52–54]. Here, we present control laws that stabilize planar formations of a school of such robotic fish (Fig. 1.2). Related work involving formation experiments of fish robots propelled by tail flapping was presented in [55, 56]. In [55], a school of fish robots achieves circular formations and other collective behaviors using vision-based behaviors based on

relative position. Similarily, in [56], parallel and circular formations are achieved using an overhead camera to provide absolute positions of all the agents. Our work differs in that we investigate synchronized motion of multiple fish robots driven by an internal reaction wheel. We utilize consensus control to achieve collective motion by communicating only relative position and/or orientation with nearby agents. This approach is particularly well suited to challenging underwater environments where small, low-power robots have limited communication or sensing range.

Figure 1.2: A school of soft robotic fish serves as a testbed for formation control experiments at the University of Maryland's Neutral Buoyancy Research Facility.

Consensus control in Euclidean space, which assumes that the states of the system live on $\mathbb{R}^N$, is a well-studied topic [57]. The goal of consensus control is to steer N agents into identical states. Similarly, average-consensus control laws steer agents towards the average value of the initial conditions of the agents [58]. Consensus and average consensus are typically studied for single-integrator dynamics [59], which may contain linear or nonlinear drift vector fields [60]. Interactions between agents can be static [61],

time-varying [62], all-to-all [61], or limited [63]. These interactions are typically described using the Laplacian matrix from algebraic graph theory [64] to compute relative state information, such as relative position. Consensus and average consensus in Euclidean space have also been studied for double-integrator dynamics [65] and second-order systems with a nonlinear drift vector field that represents the vehicle dynamics [66]. Furthermore, consensus control on a nonlinear manifold has been investigated [21, 67]. For example, consensus on the N-torus—also called synchronization—arises in the control of planar formations, where the heading orientation is a phase angle on the unit circle [19]. Orientation and translation control of agents in the plane utilizes the special Euclidean group [68]. Many synchronization approaches are based on the theory of coupled oscillators, such as the celebrated Kuramoto model [19], and invoke the graph Laplacian for cooperative control of first-order dynamics on the N-torus [20]. Second-order consensus of coupled oscillators with double-integrator dynamics [69] uses the gradient of a phase potential.

Another class of collective behaviors of multi-agent systems are circular formations. Previous work in this area studied circular formations of first-order, self-propelled particles with unit velocity. Feedback control laws designed in [19] stabilize a circular formation having a fixed center and a constant radius. Some extensions to this work consider a circular formation in a flow field [70] and constant non-unitary velocity, or with a constraint bounding the circular formation to a region of interest [71]. Other extensions include time-varying centers, so that the circular formation position is not fixed [72, 73]. Some authors assume agents use relative-position sensing to achieve circular formations around a given center and radius that is known only to a subset of agents [74]. Circular formation con-

10

trol on the tangent bundle of the N-torus has also been investigated where agents are second-order self-propelled particles [19, 69].

1.2 Contributions of this Dissertation

The contributions of this dissertation are in the areas of planar formation control for bioinspired multi-agent systems and bioinspired pursuit and evasion. These contributions provide dynamic models to study the behavioral of many biological species and validates theoretical results through experimental demonstration. Many of these results have either been published in peer-reviewed journals or submitted and are currently under review [23, 75, 76].

1.2.1 Non-overlapping Sensing and Actuation

I derive a dynamic model that describes intermittent behavior using non-overlapping sensing and actuation for a single self-propelled particle and multiple self-propelled particles with synchronous and asynchronous actuation times. Stability and bifurcation analysis of a single particle with intermittent dynamics and a closed-loop heading controller using either state or output feedback determine the effects of having non-overlapping sensing and actuation. These results are expanded to to include multiple particles with synchronous and asynchronous actuation times. I also provide practical stability bounds in the presence of bounded actuator and measurement noise for one or more particles.

1.2.2 Bioinspired Pursuit in a Structured Environment

Inspired by the predation tactics of lion fish and the common evasion strategies of prey fish, I derive a pursuer-evader interaction model with a single pursuer and a single evader in a bounded environment. The pursuer changes its morphology to aid in predation and the evader intermittently steers in a random direction to flee the pursuer. A mathematical model for the evader's escape heading probability density function in a bounded environment is also derived.

To study how the pursuer's morphology aids its predation, we use the metric of expected work to capture the evader as a function of the pursuer's shape, the relative distance between the pursuer and evader, and the evader's proximity to the boundary. I also qualitatively assess the pursuer's optimal pursuit trajectory as a function of the evader's position in a bounded environment. These results provide insight into the predation behaviors found in nature and a fundamental understanding on how a complex environment influences predation strategies.

1.2.3 Planar Formation Control for a School of Robotic Fish

The works in [43, 77] present a rigid body dynamic model for a robotic fish known as the Chaplygin sleigh and presents a closed-loop steering controller for a single robot and closed-loop heading synchronization controller for multiple robots. I experimentally validate the parallel formation control law on a school of bio-inspired robotic fish in the University of Maryland's Neutral Buoyancy Research Facility. While most of the robot's design and construction was done by a previous labmate, Jinseong Lee, I develop new

hardware, perform system identification on the robot's reaction-wheel motor dynamics, and design and implement an optimal estimation and tracking controller that follows the torque commands of the formation control.

1.3 Outline of Dissertation

This dissertation is outlined as follows. Chapter 2 reviews necessary background information and derivations for the subsequent chapters. To familiarize the reader, derivations of the dynamics for a self-propelled particle and a decentralized closed-loop steering controller for a single particle and for multiple particles are provided. A well studied kinematic pursuit model is also provided.

Chapter 3 introduces a bioinspired dynamic model for intermittent locomotion with non-overlapping sensing and actuation. This model is used to study how stability is affected by intermittent locomotion for a single particle and for a collection of multiple particles.

Chapter 4 proposes a dynamic model to study pursuit and evasion in a bounded environment with a single pursuer and a single evader. Bioinspired pursuit and evasion tactics are modeled for the pursuer and the evader, and effects of pursuit in a closed setting are studied.

Chapter 5 covers the rigid body dynamics of a robotic fish driven by an internal reaction wheel, and studies planar formation control for multiple robotic fish. Experimental demonstration of the planar formation controller validates the theory.

Chapter 2:   Background

This chapter provides background information and derivations for chapters 3-5. First, I derive the dynamic model for a single self-propelled particle with a closed-loop heading controller and discuss the stability of the closed-loop equilibrium points. Second, I introduce a decentralized steering controller to synchronize the headings of multiple particles. Third, I adapt the self-propelled particle model to have intermittent locomotion with separate sensing and actuation phases. Fourth, I introduce a kinematic pursuit model for self-propelled particles in a pursuit and evasion game. Fifth, I outline how to compute the expected value of a random variable.

2.1   Complex Variables

This dissertation uses complex numbers to express the position and orientation of the pursuer and the evader. Complex numbers have real and imaginary components and can be expressed as $h = x + jy$. The imaginary component of h is multiplied by the imaginary unit j such that $\text{Im}(h) = y$, and the real component of h is $\text{Re}(h) = x$. Since complex numbers have two components, they can be visualized in two dimensional space called the complex plane $\mathbb{C}$.

A common tool for dimension reduction is to express vectors with two orthogonal

components as a complex number. Let the horizontal and vertical position of a particle be $\boldsymbol{v} = [x, y]$, where the bold face notation represents a vector. By making the horizontal component the real axis and the vertical component the imaginary axis, we can express vector $\boldsymbol{v}$ as a complex number $v = x + jy$.

Similarly, the orientation of a vector $\boldsymbol{v}$ can be expressed as the phase of a complex number v, where the phase of v is

$$\theta = \arg(v). \tag{2.1}$$

The arg() operator is the argument of the complex number. Likewise, the magnitude of a complex number is determined by taking its absolute value.

Using the phase θ and magnitude $|v|$ of a v, we can express the position of a particle in complex polar form with Euler's formula [78], such that

$$v = |v|e^{j\theta} = |v|(\cos\theta + j\sin\theta). \tag{2.2}$$

In general, since the imaginary component is orthogonal to the real component of a complex number, multiplying that number by j rotates its phase by $\pi/2$ radians in the counterclockwise direction.

2.2 Self-propelled particle dynamics

To model planar locomotion of a moving body in a fluid, we invoke the dynamic model of a self-propelled particle. The dynamics of a self-propelled particle are useful to describe motion that distinguishes between translational acceleration (thrust) and rotational accel-

eration (turning), accomplished by expressing the particle's velocity and control inputs in polar coordinates.

Let $r_n \in \mathbb{C}$ be the position of the nth particle in the complex plane such that $r_n = x_n + jy_n$, where $x_n, y_n \in \mathbb{R}$ and j is the imaginary unit. Let $\theta_n \in \mathbf{S}^1$ and $s_n \geq 0$ be the orientation and magnitude of the particle's velocity, respectively. The drag-free self-propelled particle dynamics are [68]

$$
\begin{aligned}
\dot{r}_n &= s_n e^{j\theta_n} \\
\dot{\theta}_n &= u_n \\
\dot{s}_n &= v_n,
\end{aligned}
\tag{2.3}
$$

where u_n is the steering control and v_n is the thrust control.

To steer the particle's velocity to a desired direction θ_d, consider the control input

$$
u_n = K \sin(\theta_d - \theta_n),
\tag{2.4}
$$

where $K > 0$ is the control gain. The heading dynamics in (2.3) with control (2.4) has equilibrium points at $\theta^* = \theta_d$ and $\theta^* = \theta_d \pm \pi$. Linearization indicates that the only stable equilibrium point is $\theta^* = \theta_d$.

2.3 Multi-agent synchronization in a plane

Multi-particle formation control is a well studied topic [14, 19–22, 79]. The phase synchronization of multiple particles, also called parallel formation, with the dynamics in (2.3), is achieved by designing a steering input u_n for each of the N particles that aligns their headings to a common value. Drawing inspiration from the Kuramoto model [80] and

the noise-free steering law of the Vicsek model [14], the following steering controller uses relative heading information between the nth particle and the other particles in the school to synchronize all of their headings, [19, 21]:

$$u_n = \frac{K}{N} \sum_{m=1}^{N} \sin(\theta_m - \theta_n), \; n = 1, \cdots, N. \tag{2.5}$$

The communication protocol in (2.5) assumes each particle has knowledge of the relative headings of the other particles in the school and, because of this assumption, the school of particles has an all-to-all communication graph. The control framework extends naturally to limited communication [20].

The equilibrium points of the closed loop heading dynamics (2.3) with steering input (2.5) and constant velocity (i.e., $v_n = 0$) are classified as synchronized, balanced, and parallel anti-parallel [19]. The synchronized equilibrium point $\boldsymbol{\theta}^* = \alpha \mathbb{1}$, where $\alpha \in \mathbf{S}^1$ is the average initial heading of the particles and $\mathbb{1}$ is a vector of ones, is asymptotically stable if $K > 0$ and all other equilibrium points are unstable [19]. In Sections 3.3 and 3.4, (2.5) is used to synchronize the headings of multiple particles using state feedback with synchronous and asynchronous cycles, respectively.

2.4   Pursuit and Evasion Strategies

Pursuit and evasion are well-studied topics with applications in missile guidance [35], biological predation [30, 31, 42], and engineered systems [38, 41, 43, 44]. Pure pursuit [35], is characterized by having a pursuer P heading directly towards an evader E along their line-of-sight vector.

Let the pursuer's position be $r_P = x_P + jy_P \in \mathbb{C}$, where x_P and y_P are the horizontal and vertical positions, respectively, and j is an imaginary unit. Let θ_P and s_P be the pursuer's velocity orientation and speed, respectively. Similarly, let r_E, θ_E, and s_E be the evader's position, heading, and speed, respectively. The line-of-sight vector with respect to the pursuers body frame is

$$r_{E/P} = r_E - r_P, \tag{2.6}$$

and the orientation of the line-of-sight vector is

$$\alpha = \arg(r_{E/P}), \tag{2.7}$$

see Figure 2.1.
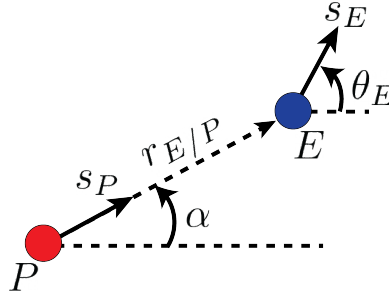
Figure 2.1: Classical pursuit model using particle kinematics

Common assumptions in the pursuit literature are that both pursuer and evader have constant speeds and that the pursuer has a higher speed than the evader [35, 36]. The ratio of the two speeds is $\varepsilon = s_P/s_E$. In the present model the pursuer's speed is arbitrarily set to $s_P = 1.05$ m/s and the evader's speed is $s_E = 1$ m/s such that $\varepsilon = 1.05$.

In pure pursuit, the time duration required to capture a non-maneuvering evader

is [35]

$$\Delta t = \frac{|r_{E/P}|}{s_E} \frac{\varepsilon + \cos(\alpha - \theta_E)}{\varepsilon^2 - 1}. \tag{2.8}$$

Note that (2.8) is only valid for $\varepsilon > 1$.

The line-of-sight orientation (2.7) is used as the reference heading for the pursuer in section 4.2, and (2.8) is used to compute the work required to capture the evader in section 4.3.

An evasion strategy observed in animals is the protean strategy [31, 32], where the evader senses the pursuer and flees in a random escape direction θ_d. The stochastic nature of this evasion strategy makes the evader less predictable to the pursuer. The random flee direction has a probability density function that depends on the evader's proximity to the boundary and relative distance to the pursuer. The probability density function of θ_d is derived in section 4.2 and used to compute the expected value of the work required to capture the evader in section 4.3.

To compute the work executed during pursuit, let T_P be the pursuer's thrust aligned with the its velocity acting at its center of mass r_P. Assuming the pursuer has a constant speed, the work that T_P does on the center of mass depends on the path the pursuer takes from some time t_0 to $t_0 + \Delta t$, where Δt is (2.8), such that [81]

$$W_P = \int_{t_0}^{t_0 + \Delta t} T_P s_P dt. \tag{2.9}$$

To find the work required to capture the evader, substitute (2.8) into (2.9) and evaluate the

19

integral such that

$$W_P = T_P |r_{E/P}| \frac{\varepsilon^2 + \varepsilon \cos(\alpha - \theta_E)}{\varepsilon^2 - 1}. \tag{2.10}$$

Note that the pursuer's work required to capture the evader depends on the evader's heading θ_E.

The randomness of the evader's protean evasion strategy makes the work in (2.10) a stochastic process and we use tools from probability theory to analyze the expected value of work, also called the expected work. In section 4.3, (2.10) is adapted to analyze the work required to capture the evader.

2.5 Expected Value of a Random Variable

To analyze the stochastic nature of a random variable, we use tools from probability theory. Let χ be a random variable on the real number line. Also let the sample space of χ be between $-\infty$ and $+\infty$, such that all possible values of χ lie between $-\infty$ and $+\infty$. The probability density function of χ is denoted by $f(\chi)$, and it describes the likelihood that χ will be within a certain range of values. To compute the expected value of χ, also known as the mean of χ, integrate the product of χ and the probability density function of over the entire sample space such that [82]

$$E[\chi] = \int_{-\infty}^{\infty} \chi f(\chi) d\chi. \tag{2.11}$$

If random variable χ is used in a function $Y = g(\chi)$ with probability density function

$f(\chi)$, then the expected value of the function is [82]

$$E[Y] = \int_{-\infty}^{\infty} g(\chi)f(\chi)d\chi. \tag{2.12}$$

We adapt (2.12) to compute the expected work required for the pursuer to capture an evader using the protean strategy in section 4.3.

Chapter 3: Estimation and Control for Collective Motion with Intermittent Locomotion

3.1 Introduction

To study the conceptual effects of separating estimation and control, I introduce a variation of Vicsek's model [14] for multiple self-propelled particles with non-overlapping actuation and sensing phases. The actuation phase, also known as the burst phase, applies thrust and steering control, whereas the sensing phase, also known as the coast phase, estimates the relative headings of other particles. In the single-particle case, the agent estimates its own heading. I also study the effects of intermittent sensing and control for multiple particles with synchronous burst phases and asynchronous burst phases.

To analyze the stability of the heading dynamics, I integrate the continuous dynamics to obtain a discrete map and use Lyapunov's indirect method. I provide conditions on system parameters that guarantee local exponential convergence to the synchronized equilibrium point using either state-feedback or output feedback for both the single-particle system and the multi-particle system with either synchronous updates or asynchronous updates. The stability conditions for a multi-particle system with asynchronous updates assumes that each group of particles have non-overlapping burst phases and constant

bounded time delays. In the presence of actuation and measurement noise, I use Lyapunov's direct method to establish practical stability bounds for the desired equilibrium point of a single particle and multiple particles.

This chapter is organized as follows. Section 3.2 introduces the intermittent dynamics of a single particle and analyzes the stability conditions of the zero-noise state and output feedback cases. Section 3.3 analyzes the stability conditions for multi-particle intermittent heading synchronization with noise-free state and output feedback with synchronous updates. Section 3.4 introduces the intermittent dynamics for a multi-particle system with asynchronous updates and analyzes the stability conditions of the zero-noise state and output feedback cases. Section 3.5 investigates the practical stability of the closed-loop heading dynamics with bounded actuation noise and measurement noise, respectively, for a single-particle and multiple particles with asynchronous cycles. Lastly, Section 3.6 summarizes the chapter and discusses ongoing and future work.

3.2   Burst and Coast Dynamics for a Single Particle

This section presents a dynamic model for a single particle with burst and coast behavior in which sensing and actuation occur during non-overlapping phases. A single burst phase combined with a single coast phase is called a cycle. Index $k = 0, 1, \ldots$ denotes the kth cycle. The duration of the burst and coast phases in a single cycle are denoted $\beta > 0$ and $\mathcal{T} > 0$, respectively, and are identical for all k. The start time of cycle k is $t_k = k(\beta + \mathcal{T})$, where $t_0 = 0$.

3.2.1 Intermittent locomotion in a fluid

The dynamics during the burst phase are adapted from (2.3). First, assume that the steering and thrust inputs for the kth burst phase, i.e., $u(t) = u(t_k)$ and $v(t) = v(t_k)$, are constant for $t \in [t_k, t_k + \beta]$. The steering input u is subject to actuator noise ξ and the particle's acceleration is subject to quadratic drag with coefficient b. The burst dynamics for cycle k are

$$\dot{r} = se^{j\theta} \tag{3.1}$$

$$\dot{\theta} = u(t_k) + \xi \tag{3.2}$$

$$\dot{s} = -bs^2 + v(t_k). \tag{3.3}$$

The values $r(t_k)$, $\theta(t_k)$, and $s(t_k)$ at the start of the kth burst phase are equal to the values of the corresponding state variables at the conclusion of the previous coast phase for $k > 0$ and equal to the initial conditions for $k = 0$.

Because there is no actuation during the coast phase, the coast dynamics are equivalent to (3.1)–(3.3) with $u(t_k) = 0$, $v(t_k) = 0$, and $\xi = 0$. Observations collected during the coast phase are denoted by y and are equal to the (constant) orientation θ of the particle velocity subject to sensor noise η. Let $\hat{\theta}$ denote the estimate of θ. The coast phase dynamics,

24

including a linear observer for θ with observer gain L, are

$$\dot{r} = se^{j\theta} \tag{3.4}$$

$$\dot{\theta} = 0 \tag{3.5}$$

$$\dot{s} = -bs^2 \tag{3.6}$$

$$\dot{\hat{\theta}} = L(y - \hat{\theta}) \tag{3.7}$$

$$y = \theta + \eta. \tag{3.8}$$

The initial conditions for coast phase k are $r(t_k + \beta)$, $\theta(t_k + \beta)$, and $s(t_k + \beta)$. Further-more, the initial heading estimate is $\hat{\theta}(t_k) = \hat{\theta}(t_{k-1})$ for $k > 0$ and $\hat{\theta}(t_k) = 0$ for $k = 0$. Figure 3.1 illustrates the dynamic model.

The output (3.8) and the observer dynamics (3.7) treat θ and $\hat{\theta}$ as linear variables in $\mathbb{R}^1$, although θ and $\hat{\theta}$ are both in S^1. To properly treat the nonlinearity of θ and $\hat{\theta}$, let $z' = e^{j\theta}$ be the position of the particle projected on the unit circle and let $y' = z'e^{j\eta} = e^{j(\theta + \eta)}$ be the noisy measured output where $\theta + \eta = \arg(y')$. Similarly, the estimated heading is $\hat{z}' = e^{j\hat{\theta}}$ and the nonlinear observer dynamics are $\dot{\hat{z}}' = jL \langle e^{j(\theta + \eta)}, e^{j\hat{\theta}} \rangle$, where $< \cdot, \cdot >$ represent the complex inner product. Evaluating the inner product and linearizing the nonlinear observer dynamics at the equilibrium point $\hat{\theta}^* = \theta$ yields $\dot{\hat{z}}' = L(\theta + \eta - \hat{\theta})$, i.e. (3.7).

3.2.2   State Feedback Heading Dynamics

For state feedback, the controls u and v are constant during the burst phase of each cycle. To track the desired heading θ_d, consider the steering control (2.4) evaluated at the
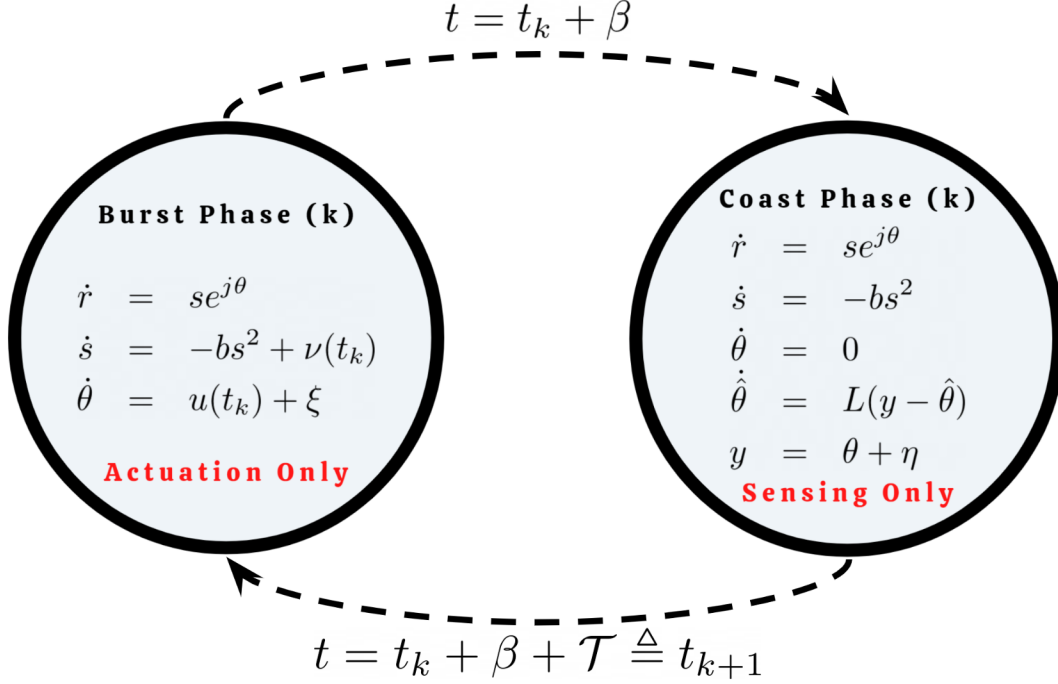
Figure 3.1: Block diagram of a single particle dynamic model with burst and coast behavior. Actuation occurs during the burst phase and sensing occurs during the coast phase.

start time t_k of burst phase k:

$$u(t_k) = K \sin(\theta_d - \theta(t_k)). \tag{3.9}$$

The thrust control during the burst phase is $v(t_k) = v_0$. This subsection characterizes the stability of the heading dynamics (3.2) with control (3.9) and no noise, i.e., $\xi = 0$; I consider the case $\xi \neq 0$ in Section 3.5.

The mapping from $\theta(t_k)$ to $\theta(t_{k+1})$ is obtained by substituting (3.9) into (3.2) and integrating from t_k to $t_k + \beta$ for the burst phase and integrating (3.5) from $t_k + \beta$ to $t_k + \beta + \mathcal{T} = t_{k+1}$ for the coast phase. I obtain

$$\theta(t_{k+1}) = f(\theta(t_k)), \tag{3.10}$$

26

where

$$f(\theta) = \theta + K\beta \sin(\theta_d - \theta). \tag{3.11}$$

The equilibrium points θ^* of the map (3.10) are the solutions to the equation $\theta = f(\theta)$, i.e., $\theta^* = \theta_d$ and $\theta^* = \theta_d \pm \pi$. To evaluate the stability of θ^*, take the Jacobian of (3.11) and evaluate it at θ^*. For $\theta^* = \theta_d$, I have

$$\left. \frac{\partial f}{\partial \theta} \right|_{\theta^* = \theta_d} = 1 - K\beta. \tag{3.12}$$

The following theorem states the necessary and sufficient conditions on the control gain K and burst duration β for $\theta^* = \theta_d$ to be an exponentially stable equilibrium point.

Theorem 3.2.1. *The map (3.11) corresponding to the closed-loop heading dynamics with noise-free state feedback exponentially stabilizes the equilibrium point $\theta^* = \theta_d$ if and only if $0 < K\beta < 2$. The equilibrium points $\theta^* = \theta_d \pm \pi$ are unstable.*

Conceptually, the technical result in Theorem 3.2.1 implies that using state feedback to steer a single particle with non-overlapping sensing and actuation to a desired heading is achievable, but the magnitude and duration of the actuation, $K\beta$, must be considered.

Proof. The proof follows from the stability condition for a linear map, which requires the eigenvalue(s) to lie within the unit circle. The map (3.10) is one dimensional and the sole eigenvalue at $\theta^* = \theta_d$ is given by (3.12). Evaluating $|1 - K\beta| < 1$, i.e., $-1 < 1 - K\beta < 1$, yields the desired result. The eigenvalue at $\theta^* = \theta_d \pm \pi$ is $1 + K\beta$, which is always greater than one because K and β are positive. □

3.2.3   Output Feedback Heading Dynamics

In the output-feedback case, θ is estimated using the linear observer (3.7) with observations (3.8). The intermittent behavior of an agent following these dynamics using output feedback is shown in Figure 3.2. The remainder of this subsection characterizes the stability of the heading dynamics (3.2) with noise-free output feedback, i.e., $\eta = 0$; I consider the case $\eta \neq 0$ in Section 3.5.
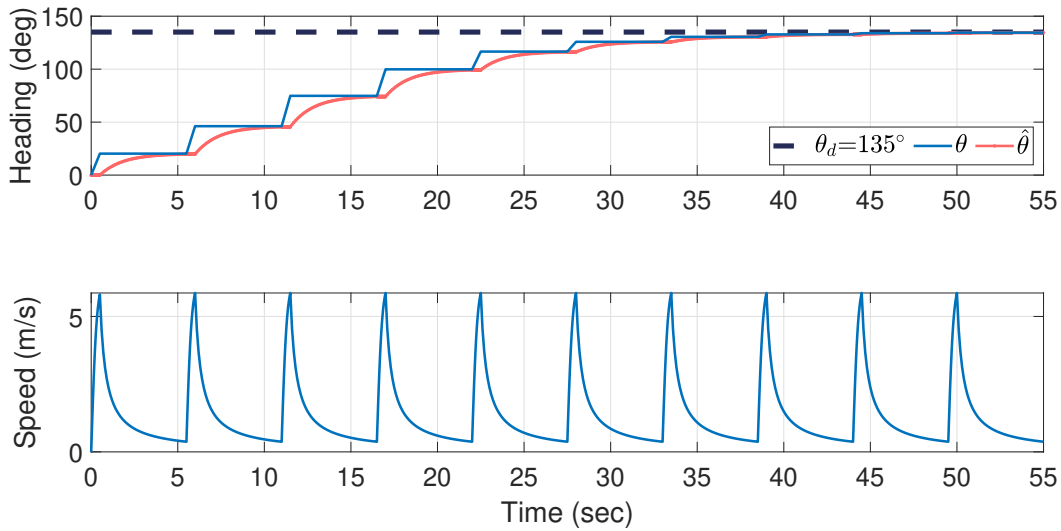
Figure 3.2: Intermittent burst and coast behavior of a single particle using output feedback to steer in the desired direction $\theta_d = 135°$.

Since output feedback control of θ utilizes the heading estimate $\hat{\theta}$, the closed-loop output feedback may be described using a two-dimensional map. Let $g(\theta, \hat{\theta})$ represent the map

$$(\theta(t_{k+1}), \hat{\theta}(t_{k+1})) = g(\theta(t_k), \hat{\theta}(t_k)), \tag{3.13}$$

where $g_1(\theta, \hat{\theta})$ denotes the map from $\theta(t_k)$ and $\hat{\theta}(t_k)$ to $\theta(t_{k+1})$ and $g_2(\theta, \hat{\theta})$ denotes the map from $\theta(t_k)$ and $\hat{\theta}(t_k)$ to $\hat{\theta}(t_{k+1})$.

Since the heading estimate $\hat{\theta}(t_k)$ is constant during the burst phase, I have

$$u(t_k) = K\sin(\theta_d - \hat{\theta}(t_k)). \qquad (3.14)$$

As with the state-feedback case, the output feedback map is

$$g_1(\theta, \hat{\theta}) = \theta + K\beta\sin(\theta_d - \hat{\theta}). \qquad (3.15)$$

The map $g_2(\theta, \hat{\theta})$ is constructed by analyzing the burst and coast phases separately. Since the heading estimate is constant during the burst phase, $\hat{\theta}(t_k + \beta) = \hat{\theta}(t_k)$. During the coast phase, $\dot{\theta} = 0$, which implies $y = \theta$ is constant from $t_k + \beta$ to $t_k + \beta + \mathcal{T}$. The map $\hat{\theta}(t_k + \beta)$ to $\hat{\theta}(t_{k+1})$ is obtained by integrating (3.7) with $\eta = 0$ to obtain

$$\hat{\theta}(t_{k+1}) = \theta(t_k + \beta)(1 - e^{-L\mathcal{T}}) + \hat{\theta}(t_k + \beta)e^{-L\mathcal{T}}. \qquad (3.16)$$

Substituting $\theta(t_k + \beta) = g_1(\theta(t_k), \hat{\theta}(t_k))$ into (3.16) and using $\hat{\theta}(t_k + \beta) = \hat{\theta}(t_k)$ yields

$$g_2(\theta, \hat{\theta}) = (1 - e^{-L\mathcal{T}})(\theta + K\beta\sin(\theta_d - \hat{\theta})) + e^{-L\mathcal{T}}\hat{\theta}. \qquad (3.17)$$

Let $z = [\theta, \hat{\theta}]^T$, which implies $z(t_{k+1}) = g(z(t_k))$, where g_1 and g_2 are given by (3.15) and (3.17), respectively. The equilibrium points of $g(z)$ are $z^* = (\theta^*, \theta^*)$, where $\theta^* = \theta_d$ or $\theta^* = \theta_d \pm \pi$. Linearizing $g(z)$ about $z^* = (\theta_d, \theta_d)$ yields the following two-dimensional linear

29

map:

$$\frac{\partial g}{\partial z}\bigg|_{z=z^*} = \begin{bmatrix} 1 & -K\beta \\ 1 - e^{-LT} & K\beta\left(e^{-LT} - 1\right) + e^{-LT} \end{bmatrix} \tag{3.18}$$

The following theorem provides conditions on the control and observer gains, K and L, and the burst and coast durations, β and T, that ensure exponential stability of the equilibrium point $z^* = (\theta_d, \theta_d)$. The other equilibrium points are unstable. The proof invokes the stability of a $2D$ map as determined by its trace and determinant [83, p. 317] (see Appendix A).

Theorem 3.2.2. *The map $g(\theta, \hat{\theta})$ given by (3.15) and (3.17) corresponding to the closed-loop heading dynamics with noise-free output feedback exponentially stabilizes the equilibrium point $(\theta^*, \hat{\theta}^*) = (\theta_d, \theta_d)$ if and only if $LT > 0$ and $0 < K\beta < \frac{2(1 + e^{-LT})}{1 - e^{-LT}}$.*

Proof. Let τ and δ be the trace and determinant of (3.18), respectively, such that

$$\tau = 1 + K\beta e^{-LT} - K\beta + e^{-LT} \tag{3.19}$$

$$\delta = e^{-LT}. \tag{3.20}$$

From (A.3), $\delta < 1$ is the first of three necessary conditions for stability of a $2D$ map. Substituting (3.20) into $\delta < 1$ and noting that $\delta > 0$ yields $0 < e^{-LT} < 1$, which implies the desired condition on the product LT. Substituting (3.19) and (3.20) into the second condition $\delta > -1 - \tau$ (A.3) yields $e^{-LT} > -2 - K\beta e^{-LT} + K\beta - e^{-LT}$, which implies

$$K\beta < \frac{2(1 + e^{-LT})}{1 - e^{-LT}}. \tag{3.21}$$

(a) $K\beta$-$L\mathcal{T}$ plane   (b) trace-determinant plane   (c) complex plane
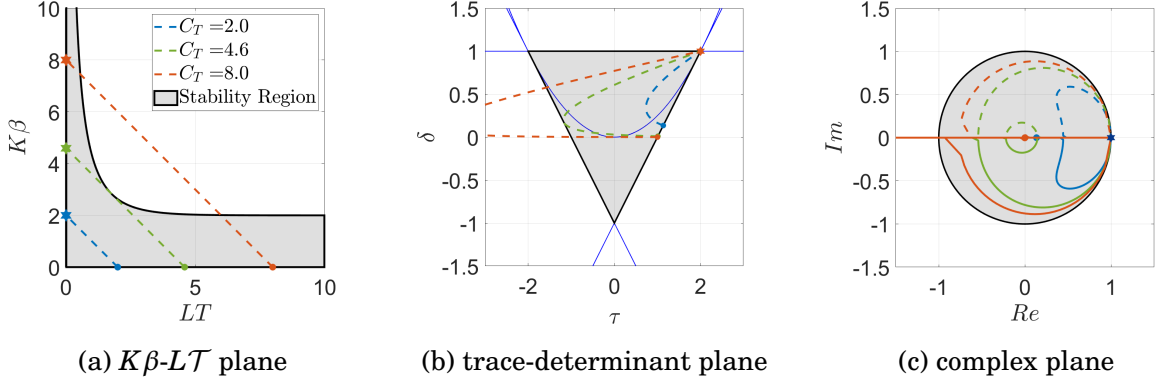
Figure 3.3: Stability regions of the burst and coast dynamics using noise-free output feedback with $K = L = 1$ and three values of the cycle time $C_T = \beta + \mathcal{T}$. The shaded regions are stable.

Substituting (3.19) and (3.20) into the third condition $\delta > -1 + \tau$ (A.3) yields $e^{-L\mathcal{T}} > K\beta e^{-L\mathcal{T}} - K\beta + e^{-L\mathcal{T}}$, which implies $K\beta > 0$ as desired. $\qquad\square$

The results of Theorem 3.2.2 are illustrated in Figures 3.3a–3.3c. Certain values of $K\beta$, $L\mathcal{T}$, and the overall cycle time $C_T = \beta + \mathcal{T}$ can destabilize the desired equilibrium point. Figure 3.3a illustrates the stability region in the $K\beta$–$L\mathcal{T}$ plane for three values of C_T; Figure 3.3b illustrates the stability region in the trace-determinant plane; Figure 3.3c illustrates the stability region in the complex plane.

Conceptually, the technical result in Theorem 3.2.2 implies that using output feedback to steer a single particle with non-overlapping sensing and actuation to a desired heading is achievable, but the strength and duration of the actuation, $K\beta$, and the observation, $L\mathcal{T}$, must be considered. Intuitively, one may expect shorter weaker bursts with longer more accurate observations to be stable. In fact this is commonly observed in a variety of biological species [3]. However, as illustrated in Figure 3.3a, the bounds on $K\beta$ and $L\mathcal{T}$ suggest that perhaps longer stronger burst with shorter less accurate observations are also stable.

3.2.4 Bifurcations of Output Feedback Dynamics

This section analyzes bifurcations of the output feedback dynamics using the total cycle time C_T as the bifurcation parameter. Solving for $\beta = C_T - \mathcal{T}$ yields the following constraint on the trajectories in the $K\beta$–$L\mathcal{T}$ plane:

$$K\beta = K(C_T - \mathcal{T}) = -\frac{K}{L}(L\mathcal{T}) + KC_T, \tag{3.22}$$

corresponding to a line with slope $-\frac{K}{L}$ and vertical-axis intercept KC_T. The following corollary to Theorem 3.2.2 identifies the largest cycle time C_T for which all values of $K\beta$ and $L\mathcal{T}$ stabilize the desired equilibrium point $\theta^* = \theta_d$.

Corollary 3.2.1. *Consider the closed-loop heading dynamics with noise-free output feedback described in Theorem 2. Let $C_T = \beta + \mathcal{T}$ denote the cycle time. The equilibrium point $\theta^* = \theta_d$ is exponentially stable for any control gain $K > 0$ and observer gain $L > 0$ if*

$$C_T < \frac{2(1+p)}{K(1-p)} + \frac{1}{L}\ln p \tag{3.23}$$

where

$$p = \frac{K + 2L + 2\sqrt{L(L+K)}}{K} \tag{3.24}$$

Proof. I seek a tangential intersection of the constraint (3.22) with the stability condition (3.21). An intersection occurs at the value of C_T for which (3.21) equals (3.22), which yields

$$C_T = \frac{2(1+e^{-L\mathcal{T}})}{K(1-e^{-L\mathcal{T}})} + \frac{1}{L}(L\mathcal{T}). \tag{3.25}$$

The intersection is tangential if the derivatives of (3.21) and (3.22) are equal at the intersection point, i.e.,

$$-\frac{K}{L} = -\frac{4e^{-L\mathcal{T}}}{(1-e^{-L\mathcal{T}})^2}.$$
(3.26)

Equation (3.26) yields the following quadratic equation in terms of $p = e^{-L\mathcal{T}}$:

$$Kp^2 - 2(K+2L)p + K = 0.$$
(3.27)

Solving for p using the quadratic equation and adopting the positive root gives the desired result. (The negative root does not satisfy the stability conditions in Theorem 3.2.2.) □

3.3 Multi-particle Synchronization with Synchronous Bursts

This section extends the intermittent dynamics of a single particle to multiple particles with all-to-all communication and synchronous cycles. I adopt the intermittent dynamics from Section 3.2 and use subscript n to denote the nth particle. First, I introduce the heading consensus controller (2.5) used to align each particle's heading. Second, I examine the equilibrium points of the multi-particle system and determine the stability properties for the state feedback case. Third, I devise an idealized sensor to observe the relative headings between each particle and determine the stability properties for the output feedback case.

3.3.1 State Feedback Heading Synchronization

As in the single-particle case, the constant thrust control input for the nth particle is $v_n = v_0$. For multiple particles, the (constant) steering input is [19]

$$u_n(t_k) = \frac{K}{N} \sum_{m=1}^{N} \sin(\theta_m(t_k) - \theta_n(t_k)), \tag{3.28}$$

which seeks to aligns each particle's heading (see Figure 3.4). The remainder of this section characterizes the stability of the heading dynamics (3.2) with (3.28) and no noise, i.e., $\xi_n = 0$. Let $\boldsymbol{\theta}$ denote the vector of headings and h_n denote the map of the nth particle's heading from $\theta_n(t_k)$ to $\theta_n(t_{k+1})$ such that $\theta_n(t_{k+1}) = h_n(\boldsymbol{\theta}(t_k))$, where

$$h_n(\boldsymbol{\theta}) = \theta_n + \frac{K\beta}{N} \sum_{m=1}^{N} \sin(\theta_m - \theta_n). \tag{3.29}$$

The synchronized equilibrium points of (3.29) are $\boldsymbol{\theta}^* = \alpha \mathbb{1}$, where $\alpha \in \boldsymbol{S}^1$ and $\mathbb{1} = [1, \cdots, 1]^T$. Linearizing (3.29) about $\boldsymbol{\theta}^*$ yields the $N \times N$ Jacobian matrix

$$\frac{\partial h_n}{\partial \boldsymbol{\theta}} \Big|_{\boldsymbol{\theta}=\boldsymbol{\theta}^*} = \begin{cases} 1 - \dfrac{K\beta}{N}(N-1) & n = m \\ \dfrac{K\beta}{N} & n \neq m \end{cases}. \tag{3.30}$$

The following theorem provides conditions on $K\beta$ for $\boldsymbol{\theta}^* = \alpha \mathbb{1}$ to be exponentially stable. Note the result is identical to the single-particle case.

Theorem 3.3.1. *The map* (3.29) *corresponding to the multi-particle closed-loop heading dynamics with noise-free state feedback exponentially stabilizes the synchronized equilibrium*
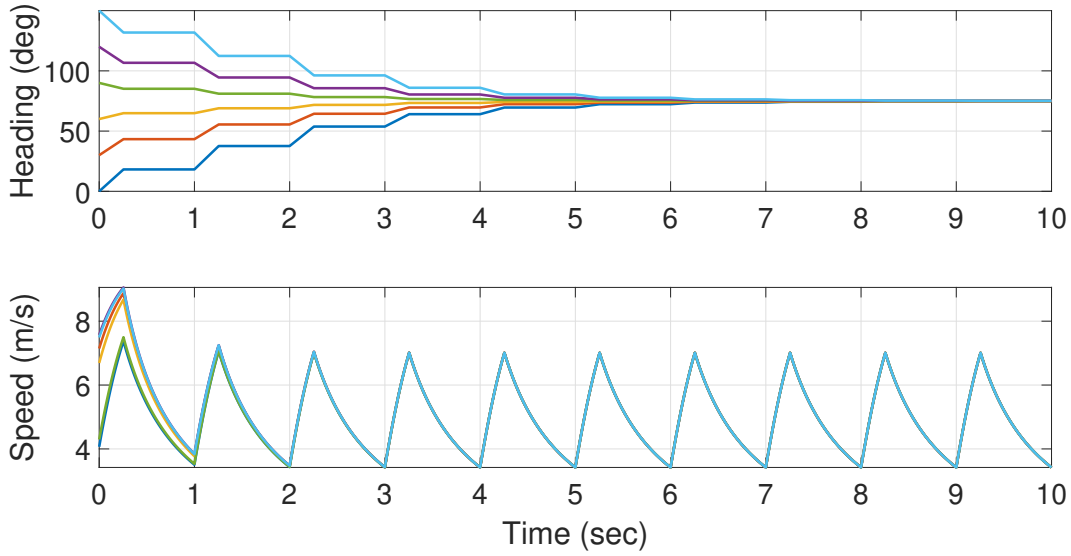
Figure 3.4: State feedback heading alignment for multiple particles with intermittent behavior.

point if and only if $0 < K\beta < 2$.

Proof. Let there be N agents such that the Jacobian matrix follows the structure of (3.30). The eigenvalues of (3.30) are $\lambda = 1$ and $N - 1$ repeated roots of $\lambda = 1 - K\beta$. Evaluating the magnitude of the repeated eigenvalues to be less then 1, i.e., $-1 < 1 - K\beta < 1$, yields the desired result. The eigenvector for the $\lambda = 1$ eigenvalue corresponds to the inertial frame's rotational symmetry and does not affect the convergence to $\boldsymbol{\theta}^*$. All other equilibrium points are unstable [19]. □

3.3.2 Output Feedback Heading Alignment

To simplify notation, let the relative headings between the mth and nth particles be denoted by $\theta_{m,n} = \theta_m - \theta_n$ and let $\boldsymbol{\Delta\theta} = [\theta_{1,2}, \cdots, \theta_{N,N-1}]^T$ be the $N^2 - N$ vector of relative headings for N particles. The output equation and linear observer dynamics for the multi-

particle coast phase are

$$y = \Delta\boldsymbol{\theta} + \boldsymbol{\eta} \tag{3.31}$$

and

$$\Delta\dot{\hat{\boldsymbol{\theta}}} = L\left(y - \Delta\hat{\boldsymbol{\theta}}\right), \tag{3.32}$$

respectively, where L is the observer gain and $\Delta\hat{\boldsymbol{\theta}}$ is the vector of estimated relative headings.

In the output-feedback case I use an idealized sensor to estimate the relative headings $\Delta\boldsymbol{\theta}$ during the coast phase. The estimated relative headings $\Delta\hat{\boldsymbol{\theta}}$ are used in the steering control input during the burst phase. The heading controller during the burst phase is

$$u_n = \frac{K}{N} \sum_{m=1}^{N} \sin(\hat{\theta}_{m,n}(t_k)). \tag{3.33}$$

Since (3.33) utilizes $\hat{\theta}_{m,n}(t_k)$, the closed-loop heading dynamics may be described using a N^2-dimensional map. Let $H(\boldsymbol{\theta}, \Delta\hat{\boldsymbol{\theta}})$ represent the map so that

$$(\boldsymbol{\theta}(t_{k+1}), \hat{\boldsymbol{\theta}}(t_{k+1})) = H(\boldsymbol{\theta}(t_k), \Delta\hat{\boldsymbol{\theta}}(t_k)), \tag{3.34}$$

where $H_\theta(\boldsymbol{\theta}, \Delta\hat{\boldsymbol{\theta}})$ denotes the map from $\theta_n(t_k)$ and $\Delta\hat{\boldsymbol{\theta}}_n(t_k)$ to $\theta_n(t_{k+1})$ and $H_{\Delta\theta}(\boldsymbol{\theta}, \Delta\hat{\boldsymbol{\theta}})$ denotes the map from $\theta_n(t_k)$ and $\Delta\hat{\boldsymbol{\theta}}_n(t_k)$ to $\Delta\hat{\boldsymbol{\theta}}_n(t_{k+1})$.

The nth term of the multi-particle output feedback map is

$$H_\theta^n(\boldsymbol{\theta}, \Delta\hat{\boldsymbol{\theta}}) = \theta_n + \frac{K\beta}{N} \sum_{m=1}^{N} \sin\left(\hat{\theta}_{m,n}\right). \tag{3.35}$$

The map $H_{\Delta\theta}(\boldsymbol{\theta}, \Delta\hat{\boldsymbol{\theta}})$ is determined by integrating (3.32), substituting (3.35), and using $\theta_{m,n}(t_k + \beta) = \theta_{m,n}(t_{k+1})$, which yields the (m, n)th term of

$$H_{\Delta\theta}^{m,n}(\boldsymbol{\theta}, \hat{\boldsymbol{\theta}}) = (1 - e^{-L\mathcal{T}})\left(\theta_{m,n} + u_m - u_n\right) + e^{-L\mathcal{T}}\hat{\theta}_{m,n}, \tag{3.36}$$

where u_m and u_n are given by (3.33) for the mth and nth particles, respectively.

Let $\boldsymbol{\phi} = [\boldsymbol{\theta}, \Delta\hat{\boldsymbol{\theta}}]^T$ represent the N^2-dimensional column vector of the absolute headings and estimated relative headings. This implies that $\boldsymbol{\phi}(t_{k+1}) = H(\boldsymbol{\phi}(t_k))$, where H_θ and $H_{\Delta\theta}$ are given by (3.35) and (3.36), respectively. The synchronized equilibrium points of $H(\boldsymbol{\phi})$ are $\boldsymbol{\phi}^* = [\boldsymbol{\theta}^*, \Delta\hat{\boldsymbol{\theta}}^*]^T$, where $\boldsymbol{\theta}^* = \alpha\mathbb{1}$ and $\Delta\hat{\boldsymbol{\theta}}^* = \mathbf{0}$.

Linearizing $H(\boldsymbol{\phi})$ about the synchronized equilibrium points yields a $N^2 \times N^2$ Jacobian matrix

$$\left.\frac{\partial H}{\partial \boldsymbol{\phi}}\right|_{\boldsymbol{\phi}=\boldsymbol{\phi}^*} = \left.\begin{bmatrix} \frac{\partial H_\theta}{\partial \boldsymbol{\theta}} & \frac{\partial H_\theta}{\partial \Delta\hat{\boldsymbol{\theta}}} \\ \frac{\partial H_{\Delta\theta}}{\partial \boldsymbol{\theta}} & \frac{\partial H_{\Delta\theta}}{\partial \Delta\hat{\boldsymbol{\theta}}} \end{bmatrix}\right|_{\boldsymbol{\phi}=\boldsymbol{\phi}^*}. \tag{3.37}$$

Evaluating (3.37) for $N = 2$ particles yields

$$\frac{\partial H_\theta}{\partial \boldsymbol{\theta}} = \begin{bmatrix} 1 & 0 \\ 0 & 1 \end{bmatrix}, \quad \frac{\partial H_\theta}{\partial \Delta\hat{\boldsymbol{\theta}}} = \begin{bmatrix} \frac{K\beta}{2} & 0 \\ 0 & \frac{K\beta}{2} \end{bmatrix}, \quad \frac{\partial H_{\Delta\theta}}{\partial \boldsymbol{\theta}} = \begin{bmatrix} e^{-L\mathcal{T}} - 1 & 1 - e^{-L\mathcal{T}} \\ 1 - e^{-L\mathcal{T}} & e^{-L\mathcal{T}} - 1 \end{bmatrix},$$

$$\frac{\partial H_{\Delta\theta}}{\partial \Delta\hat{\boldsymbol{\theta}}} = \begin{bmatrix} e^{-L\mathcal{T}} + \frac{1}{2}\left(K\beta(e^{-L\mathcal{T}} - 1)\right) & -\frac{1}{2}\left(K\beta(e^{-L\mathcal{T}} - 1)\right) \\ -\frac{1}{2}\left(K\beta(e^{-L\mathcal{T}} - 1)\right) & e^{-L\mathcal{T}} + \frac{1}{2}\left(K\beta(e^{-L\mathcal{T}} - 1)\right) \end{bmatrix}.$$

The evaluation of (3.37) for $N = 3$ particles followed a similar structure, and the general

37

form of (3.37) for N particles with noise-free output feedback is

$$\frac{\partial H}{\partial \phi}\bigg|_{\phi=\phi^*} = \begin{bmatrix} I & A \\ D & e^{-L\mathcal{T}}I + DA \end{bmatrix},\tag{3.38}$$

where I is the identity matrix of appropriate dimensions, $A \in \mathbb{R}^{N \times N^2 - N}$ is a block diagonal matrix with $N-1$ repeated $\frac{K\beta}{N}$ entries on the diagonal, and $D \in \mathbb{R}^{N^2-N \times N}$ is the transpose of incidence matrix [79] of an all-to-all communication network multiplied by $(e^{-L\mathcal{T}} - 1)$.

As an example, the A and D matrices for $N = 3$ particles are

$$A = \frac{K\beta}{N}\begin{bmatrix} 1 & 1 & 0 & 0 & 0 & 0 \\ 0 & 0 & 1 & 1 & 0 & 0 \\ 0 & 0 & 0 & 0 & 1 & 1 \end{bmatrix}, \quad D = \left(e^{-L\mathcal{T}} - 1\right)\begin{bmatrix} 1 & -1 & 0 \\ 1 & 0 & -1 \\ -1 & 1 & 0 \\ 0 & 1 & -1 \\ -1 & 0 & 1 \\ 0 & -1 & 1 \end{bmatrix}.$$

The following theorem provides conditions on the products $K\beta$ and $L\mathcal{T}$ that exponentially stabilize the synchronized equilibrium point for N particles. The other equilibrium points are unstable. Note, the following result matches the single particle case.

Theorem 3.3.2. *The map $H(\theta, \Delta\hat{\theta})$ given by (3.35) and (3.36) corresponding to the closed-loop heading dynamics with noise-free output feedback exponentially stabilizes the synchronized equilibrium point if and only if $L\mathcal{T} > 0$ and $0 < K\beta < \frac{2(1+e^{-L\mathcal{T}})}{1-e^{-L\mathcal{T}}}$.*

Proof. Let λ be the eigenvalues of the linearized heading dynamics (3.37) for N particles,

such that there is a single eigenvalue at $\lambda = 1$, there are $N^2 - 2N + 1$ eigenvalues at $\lambda = e^{-L\mathcal{T}}$, and there are $N - 1$ eigenvalue pairs at

$$\lambda = \frac{1}{2}\left(\left(e^{-L\mathcal{T}}(1+K\beta)+(1-K\beta)\right) \pm \sqrt{\left(e^{-L\mathcal{T}}(1+K\beta)+(1-K\beta)\right)^2 - 4e^{-L\mathcal{T}}}\right). \qquad (3.39)$$

For a map to be exponentially stable, λ must lie within the unit circle centered at the origin of the complex plane, i.e, $|\lambda| < 1$. For the repeated $\lambda = e^{-L\mathcal{T}}$ eigenvalues, the stability condition yields $e^{-L\mathcal{T}} < 1$, which implies the desired condition on the product $L\mathcal{T}$. Similarly, evaluating the stability of (3.39) yields $(K\beta + 2)(e^{-L\mathcal{T}} - 1) > -4$, which implies

$$K\beta < \frac{2(1+e^{-L\mathcal{T}})}{1 - e^{-L\mathcal{T}}}. \qquad (3.40)$$

The eigenvector for the $\lambda = 1$ eigenvalue corresponds to the rotational symmetry of the inertial frame and does not affect convergence to $\boldsymbol{\phi}^* = [\alpha\mathbb{1}, \mathbf{0}]^T$. $\qquad\square$

3.4   Heading Synchronization with Asynchronous Updates

This section examines the intermittent heading synchronization of multiple particles with asynchronous cycles. The asynchronous assumption implies that the burst phases for individual particles can occur at different times. To generalize the intermittent dynamics for multiple particles with asynchronous cycles, I build on the work from [22]. In [22] it is assumed that the particles share a fixed communication graph, all particles are actuated over a uniform time horizon (i.e., all particles have constant and equivalent cycle times), and only non-connected particles can burst at the same time. I relax this last assumption

by introducing the concept of groups. I define a group as a collection of particles with distinct initial conditions that burst at the same time. To model the ensemble level dynamics for a collection of particles with asynchronous intermittent locomotion, I introduce a time-dependent matrix $B(t)$ that selects which particles are bursting at time t. I also introduce a constraint on the delays between each group's burst phase and assume that groups have distinct burst phases. While the non-overlapping burst phase assumption may seem artificial, the duration of the burst phase for many aquatic species is small relative to the duration of the coast phase [3]. Therefore, I are assuming that the duration of the burst phase for one group is small enough to not overlap with the burst phase of another group. With these assumptions, I examine the stability of the synchronized equilibrium point and determine stability criteria for the state feedback case. For the output feedback case, I use the idealized sensor from Section 3.3 to determine the stability properties for the synchronized equilibrium point.

3.4.1 Modeling Intermittent Group Dynamics

Let $\mathbf{x} = [r_1 \cdots r_N, s_1 \cdots s_N, \theta_1 \cdots \theta_N]^T$ denote the vector of states for N self-propelled particles and $\mathbf{y}_n$ be the output vector of relative headings for the nth particle. Using the framework described in Section 3.2, the dynamics during the burst and coast phases are $\dot{\mathbf{x}} = f_b(\mathbf{x}, \mathbf{u}, v)$ and $\dot{\mathbf{x}} = f_c(\mathbf{x})$, respectively, where the burst dynamics for the nth agent are

$$f_b^n(\mathbf{x}, \mathbf{u}, v) = \begin{cases} \dot{r}_n = s_n e^{j\theta_n} \\ \dot{\theta}_n = u_n(t_k) \\ \dot{s}_n = v_n(t_k) - b s_n^2, \end{cases} \tag{3.41}$$

40

and the coast dynamics for the nth particle are

$$f_c^n(\mathbf{x}) = \begin{cases} \dot{r}_n = s_n e^{j\theta_n} \\[1.5ex] \dot{\theta}_n = 0 \\[1.5ex] \dot{s}_n = -b s_n^2 \\[1.5ex] \mathbf{y}_n = \theta_m - \theta_n, \quad \forall\, m \neq n \\[1.5ex] \dot{\hat{\theta}}_n = L(\mathbf{y} - \hat{\mathbf{y}}), \end{cases} \tag{3.42}$$

where the constant input u_n is (3.28) and $v_n = v_0$ for all $n = 1, \dots, N$.

The dynamics for the collection of particles at any given time can be written as

$$\dot{\mathbf{x}} = B(t) f_b(\mathbf{x}, \mathbf{u}, v) + (I - B(t)) f_c(\mathbf{x}), \tag{3.43}$$

where $B(t)$ is a diagonal matrix that selects which of the P subset groups of particles are bursting. The following assumptions are used to define the structure and piecewise time dependence of $B(t)$. First, assume that the particles are homogeneous, in that all particles coast for T seconds and burst for β seconds. Second, assume that the particles have non-overlapping burst phases separated by delays.

Let $d_{p/p-1}$ be the delay between the p and $p-1$ groups and let $\mathbf{d} \in \mathbb{R}^P$ be the vector of subsequent delays between each particle group, such that

$$\mathbf{d} = [d_{1/0}, d_{2/1}, d_{3/2}, \dots, d_{P/P-1}]^T, \tag{3.44}$$

where $d_{1/0}$ is the delay between the start of the global cycle time $t = t_k$ and the start of

41

the first group's burst phase. Assume that $d_{1/0} = 0$, without loss of generality. Since the particles have non-overlapping bursts, the sum of the delays between each group's burst phase must be in the following range

$$0 \leq \mathbb{1}^T \mathbf{d} \leq C_T - P\beta. \tag{3.45}$$

Due to the delays between the burst phases of each particle group, the burst phase of all particles does not start at t_k. Instead, the beginning of the burst phase for the particles in the pth group is

$$\tau_k^p = t_k + (p-1)\beta + \sum_{m=1}^{p} d_{m/m-1}, \tag{3.46}$$

and the end of the coast phase for the pth group is

$$\tau_{k+1}^p = t_k + p\beta + \mathcal{T} + \sum_{m=1}^{p} d_{m/m-1}. \tag{3.47}$$

Note that τ_k^p and τ_{k+1}^p are universal times among all particles, but the status of whether or not a group is bursting depends on the value of $B(t)$.

Let $\mathbb{V}$ be the set of N particles such that $\mathbb{V} = \{1, \ldots, N\}$, $\mathcal{E}_p$ be the set of particles in the pth group where $\mathcal{E}_p \subseteq \mathbb{V}$, and $\psi_p \in \mathbb{R}^{N \times N}$ be the diagonal matrix that represents the pth particle group in the school of N particles. The nth element on the main diagonal in ψ_p is either a 1 or 0 depending on whether the nth particle is in $\mathcal{E}_p$. Generally the nth diagonal
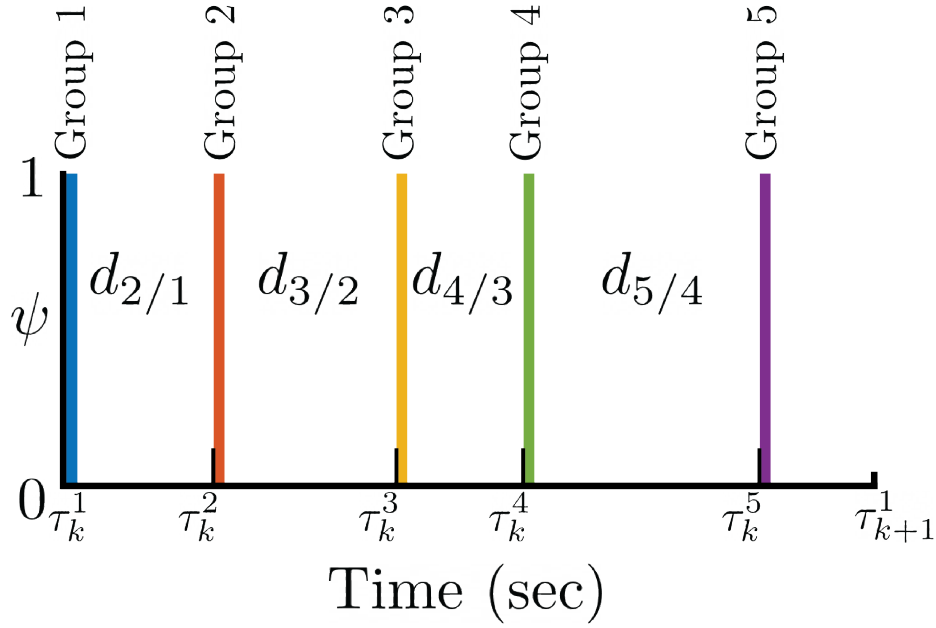
Figure 3.5: Timeline of asynchronous intermittent locomotion for $P = 5$ groups with delays between burst phases. When $\psi_p = 1$, particle group p is bursting, whereas when $\psi_p = 0$ group p is coasting.

entry of ψ_p can be expressed as

$$
\psi_p^n =
\begin{cases}
1, & \text{if } n \in \mathcal{E}_p, \\
0, & \text{otherwise.}
\end{cases}
\tag{3.48}
$$

Figure 3.5 illustrates a timeline of the school's behavior for $P = 5$ groups.

3.4.2 State Feedback Heading Synchronization with Asynchronous Bursts

For the state feedback case with asynchronous cycles, $B(t)$ is expressed as

$$
B(t) =
\begin{cases}
I \otimes \psi_p; & \tau_k^p \leq t \leq \tau_k^p + \beta \\
\mathbf{0}; & \text{otherwise}
\end{cases}
,
\tag{3.49}
$$

where $\mathbf{0}$ is a matrix of zeros with the appropiate dimensions. In (3.49), the Kronecker product $\otimes$ with $I \in \mathbb{R}^{P \times P}$ is used to distribute ψ_p among all N particles such that

$$
B(t) = \begin{bmatrix} \psi_p(t) & 0 & 0 & \cdots & 0 \\ 0 & \psi_p(t) & 0 & \cdots & 0 \\ 0 & 0 & \psi_p(t) & \cdots & 0 \\ \vdots & \vdots & \vdots & \ddots & \vdots \\ 0 & 0 & 0 & \cdots & \psi_p(t) \end{bmatrix} \in \mathbb{R}^{PN \times PN}
\tag{3.50}
$$

from $\tau_k^p \leq t \leq \tau_k^p + \beta$.

Let $b_n(t)$ be the element of $B(t)$ corresponding to the nth particle, such that

$$
b_n(t) = \begin{cases} \psi_p^n, & \tau_k^p \leq t \leq \tau_k^p + \beta, \\ 0, & \text{otherwise.} \end{cases}
\tag{3.51}
$$

The closed-loop heading dynamics of the nth particle with control law (3.28) synchronizes the headings of the particles with asynchronous state feedback (see Figure 3.6). The closed-loop heading dynamics are

$$
\dot{\theta}_n = b_n(t) \left(\frac{K}{N} \sum_{m=1}^{N} \sin(\theta_m(\tau_k) - \theta_n(\tau_k)) \right) + (1 - b_n(t))(0).
\tag{3.52}
$$

Note that if the nth particle is in the pth group, then $b_n(t) = 1$ from $\tau_k^p \leq t \leq \tau_k^p + \beta$ and
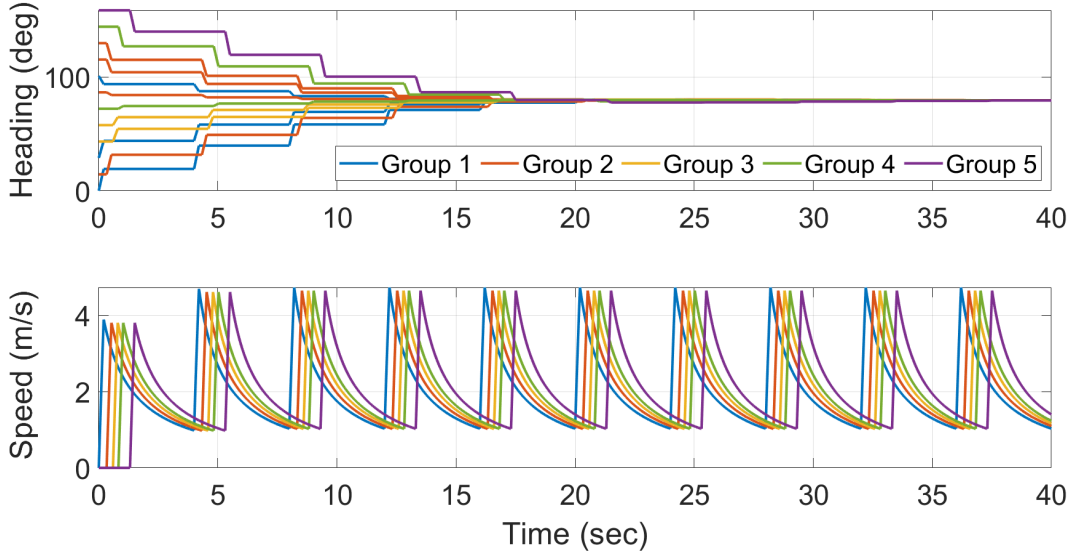
Figure 3.6: Asynchronous convergence to the synchronized heading equilibrium point for a collection of N=12 agents and P=5 groups using state feedback. Since distinct groups of particles have non-overlapping burst phases, their respective speeds will never synchronize as time goes to infinity, as in the previous section.

$b_n(t) = 0$ for the remainder of the cycle. Integrating (3.52) from the τ_k^p to τ_{k+1}^p yields

$$\int_{\theta_n(\tau_k^p)}^{\theta_n(\tau_{k+1}^p)} d\theta_n = \int_{\tau_k^p}^{\tau_k^p + \beta} b_n(t) \Big(\frac{K}{N} \sum_{m=1}^{N} \sin\big(\theta_m\big(\tau_k^p\big) - \theta_n\big(\tau_k^p\big)\big)\Big) dt + \int_{\tau_k^p + \beta}^{\tau_{k+1}^p} 0 \, dt \tag{3.53}$$

$$\theta_n\big(\tau_{k+1}^p\big) = \theta_n\big(\tau_k^p\big) + \frac{K\beta}{N} \sum_{m=1}^{N} \sin\big(\theta_m\big(\tau_k^p\big) - \theta_n\big(\tau_k^p\big)\big). \tag{3.54}$$

Note that (3.54) is identical to the state feedback case with synchronous cycles.

The following theorem provides conditions that guarantee local exponential convergence to the synchronized equilibrium point $\boldsymbol{\theta}^* = \alpha \mathbb{1}$.

Theorem 3.4.1. *The map* (3.54) *corresponding to the closed-loop heading dynamics with noise-free asynchronous state feedback locally exponentially stabilizes the synchronized equilibrium point if and only if the constraint in* (3.45) *is satisfied and* $0 < K\beta < 2$.

45

Proof. Given that the delay vector $\boldsymbol{d}$ satisfies the constraint in (3.45), the map (3.54) corresponding to the closed-loop heading dynamics with noise-free asynchronous state feedback is identical to the map (3.29) corresponding to the closed-loop heading dynamics with noise-free synchronous state feedback. The Jacobian matrix of (3.54) for N particles is (3.30). The remainder of the proof follows the proof of Theorem 3.3.1. □

3.4.3 Output Feedback Heading Synchronization

For the output feedback case with asynchronous cycles, I use the control law (3.33) to synchronize the headings of the particles and the measurements (3.32) to estimate the relative headings between particles. Since I are measuring the relative headings for each of the particles, the structure of the $B(t)$ matrix differs from the state feedback case. The ψ_p matrix for the pth particle group is (3.48); however, distributing ψ_p with the Kronecker product of the identity matrix is required such that

$$B(t) \;=\; \begin{cases} \begin{bmatrix} \psi_p & 0 \\ 0 & \psi_p \otimes I \end{bmatrix}, & \tau_k^p \le t \le \tau_k^p + \beta, \\[2em] \mathbf{0}, & \text{otherwise} \end{cases} \tag{3.55}$$

The closed-loop heading dynamics for the nth particle are

$$\dot{\theta}_n = b_n(t)\left(\frac{K}{N}\sum_{m=1}^{N}\sin\left(\hat{\theta}_{m,n}\right)\right) + (1-b_n(t))(0), \tag{3.56}$$

and the estimated relative heading observer dynamics are

$$\Delta\dot{\hat{\boldsymbol{\theta}}}_n = b_n(t)(0) + (1 - b_n(t))\big(L(\Delta\boldsymbol{\theta}_n - \Delta\hat{\boldsymbol{\theta}}_n)\big). \tag{3.57}$$

I derive the map for the closed-loop heading dynamics by using separation of variables and integrating (3.56) from $t = \tau_k^p$ to $t = \tau_{k+1}^p$, which yields

$$\theta_n\big(\tau_{k+1}^p\big) = \theta_n\big(\tau_k^p\big) + \frac{K\beta}{N}\sum_{m=1}^{N}\sin\big(\hat{\theta}_{m,n}\big(\tau_k^p\big)\big). \tag{3.58}$$

The map for the observer dynamics is derived by integrating (3.57) from τ_k^p to τ_{k+1}^p and substituting in (3.58), yielding

$$\hat{\theta}_{m,n}\big(\tau_{k+1}^p\big) = (1 - e^{-L\mathcal{T}})\big(\theta_{m,n}\big(\tau_k^p\big) + u_m\big(\tau_k^p\big) - u_n\big(\tau_k^p\big)\big) + e^{-L\mathcal{T}}\hat{\theta}_{m,n}\big(\tau_k^p\big), \tag{3.59}$$

where u_m and u_n are the heading inputs for the mth and nth particles, respectively. Note that (3.58) and (3.59) are identical to the maps (3.35) and (3.36). The following theorem provides sufficient conditions to exponentially stabilize the synchronized equilibrium point $\boldsymbol{\phi}^*$.

Theorem 3.4.2. *The maps* (3.58) *and* (3.59) *corresponding to the closed-loop heading dynamics with noise-free asynchronous output feedback locally exponentially stabilizes the synchronized point if the constraint in* (3.45) *is satisfied, $L\mathcal{T} > 0$, and $0 < K\beta < \frac{2(1 + e^{-L\mathcal{T}})}{1 - e^{-L\mathcal{T}}}$.*

Proof. Given that the delay vector $\boldsymbol{d}$ satisfies the constraint in (3.45), the maps (3.58) and (3.59) corresponding to the closed-loop heading dynamics and estimation with noise-free

asynchronous output feedback, respectively, are identical to the maps (3.35) and (3.36), corresponding to the closed-loop heading dynamics and estimation with noise-free synchronous output feedback, respectively. The Jacobian matrix of (3.58) and (3.59) for N particles is (3.37). The remainder of the proof follows the proof of Theorem 3.3.2. □

A common assumption in decentralized consensus and synchronization literature is homogeneous control parameters [20–22]. In the present work, the particles share a common control gain K, burst duration β, and observer gain L. However, if the particles had different burst durations, then one could implement an additional consensus controller to achieve a common β before synchronizing the particle's headings. After aligning β for all particles the simulations would be equivalent to the results presented in this chapter.

3.5   Noisy Sensing and Actuation

This section considers the robustness of the estimation and control results from Sections 3.2 − 3.4 under the influence of sensor and actuator noise. First, Lyapunov analysis (see Appendix) shows that the synchronized equilibrium point is uniformly ultimately bounded under the dynamics (3.2) with state-feedback heading control (3.9) for a single particle and (3.28) for multiple particles and bounded actuator noise $\xi \neq 0$. Second, a similar analysis shows that the estimation error $\sigma = \theta - \hat{\theta}$ is uniformly ultimately bounded under the observer dynamics (3.7) with observation (3.8) and bounded measurement noise $\eta \neq 0$.

3.5.1 State Feedback Noisy Heading Control

Consider the single particle heading dynamics (3.2) with state-feedback control (3.9) and bounded actuator noise ξ. Let $q = \theta - \theta_d$ denote the smallest angular difference between θ and θ_d. The map from $q(t_k)$ to $q(t_{k+1})$ is obtained from $f(\theta)$ in (3.11) by including $\bar{\xi} = \int_{t_k}^{t_k+\beta} \xi dt$ on the right-hand side and subtracting θ_d from both sides. Assume $|\bar{\xi}| \leq \gamma$. Taking the Taylor series expansion of $\sin q$ about $q = 0$ yields

$$q(t_{k+1}) = q(t_k) - K\beta q(t_k) + \bar{\xi}. \tag{3.60}$$

Consider a quadratic Lyapunov function candidate $V(q) = \frac{1}{2}q^2$. Let $\Delta V(t_k) = V(t_{k+1}) - V(t_k)$. Along solutions of the map (3.60), I have

$$
\begin{aligned}
\Delta V &= \frac{1}{2}K\beta(K\beta - 2)q^2 + (1 - K\beta)q\bar{\xi} + \frac{1}{2}\bar{\xi}^2 \\
&\leq \frac{1}{2}K\beta(K\beta - 2)q^2 + |1 - K\beta||q|\gamma + \frac{1}{2}\gamma^2
\end{aligned}
\tag{3.61}
$$

The following corollary to Theorem 3.2.1 identifies a bound on q proportional to the actuator noise bound γ.

Corollary 3.5.1. *Consider the closed-loop heading dynamics (3.2) with noisy state feedback $\xi \neq 0$. Let $\bar{\xi} = \int_{t_k}^{t_k+\beta} \xi dt$ for all k. Assume $0 < K\beta < 2$, and $|\bar{\xi}| < \gamma$. The solution $\theta(t)$ is uniformly ultimately bounded with bound $\theta_d \pm \frac{\gamma}{K\beta}$.*

Proof. Since $0 < KB < 2$, (3.61) corresponds to a concave-down parabola $\Delta V(q)$. Therefore, $V(q)$ is decreasing for all values of q for which $\Delta V < 0$. The roots $\Delta V = 0$ occur for $q =$

$\frac{\gamma}{K\beta}$, $\frac{\gamma}{K\beta-2}$, which implies solutions converge to $|q| < \frac{\gamma}{K\beta}$. □

For the multi-particle case, with either synchronous or asynchronous cycles, consider the map of the nth particle's closed-loop heading dynamics (3.54) with bounded actuator noise $\bar{\xi}_n = \int_{\tau_k^p}^{\tau_{k+1}^p} \xi_n dt$. Let the smallest difference between the nth and mth particle headings at time τ_k^p be $\theta_{nm}(\tau_k^p)$. The map from $\theta_{nm}(\tau_k^p)$ to $\theta_{nm}(\tau_{k+1}^p)$ is

$$\theta_{nm}(\tau_{k+1}^p) = \theta_{nm}(\tau_k^p) + \frac{K\beta}{N} \sum_{q=1}^{N} \left(\sin\left(\theta_q(\tau_k^p) - \theta_n(\tau_k^p)\right) - \sin\left(\theta_q(\tau_k^p) - \theta_m(\tau_k^p)\right) \right) + \left(\bar{\xi}_n - \bar{\xi}_m\right).$$

(3.62)

Taking a Taylor series expansion about $\theta_{nm} = 0$ yields

$$\theta_{nm}(\tau_{k+1}^p) = \theta_{nm}(\tau_k^p) - K\beta\theta_{nm}(\tau_k^p) + \left(\bar{\xi}_n - \bar{\xi}_m\right). \qquad (3.63)$$

Consider the quadratic Lyapunov function candidate $V(\boldsymbol{\theta}) = \frac{N}{2} \sum_{q=1}^{N} \sum_{a=1}^{N} \theta_{qa}^2(\tau_k^p)$. Let $\Delta V(\tau_k^p) = V(\tau_{k+1}^p) - V(\tau_k^p)$ and assume $|\bar{\xi}_n| \le \gamma$. Along solutions of the map (3.62), I have

$$\Delta V = \frac{N}{2} \sum_{q}^{N} \sum_{a}^{N} \left(K\beta\left(K\beta-2\right)\right)\theta_{qa}^2(\tau_k^p) + 2\left(1-K\beta\right)\left(\bar{\xi}_q - \bar{\xi}_a\right)\theta_{qa}(\tau_k^p) + \left(\bar{\xi}_q - \bar{\xi}_a\right)^2$$

$$\Delta V \le \frac{N}{2} \sum_{q=1}^{N} \sum_{a=1}^{N} \left(K\beta\left(K\beta-2\right)\right)\theta_{qa}^2(\tau_k^p) + 2\left|1-K\beta\right|\left(2\gamma\right)\left|\theta_{qa}(\tau_k^p)\right| + \left(2\gamma\right)^2 \qquad (3.64)$$

The following corollary to Theorem 3.4.1 identifies the bound on θ_{nm} proportional to the magnitude of actuator noise γ.

Corollary 3.5.2. *Consider the closed-loop multi-particle heading dynamics (3.52) with noisy state feedback $\xi_n \neq 0$. Let $\bar{\xi}_n = \int_{\tau_k^p}^{\tau_k^p + \beta} \xi_n dt$ for all k. Assume $0 < K\beta < 2$, and $|\bar{\xi}_n| < \gamma$.*

50

The solution $\boldsymbol{\theta}(t)$ is uniformly ultimately bounded with bound $\alpha\mathbb{1} \pm \frac{\gamma}{K\beta}$.

Proof. Since $0 < K\beta < 2$, (3.64) corresponds to a sum of concave-down parabolas $\Delta V(\boldsymbol{\theta})$. Therefore, $V(\boldsymbol{\theta})$ is decreasing for all values of θ_{qa} for which $\Delta V < 0$. The roots $\Delta V = 0$ occur for $\theta_{qa} = \frac{\gamma}{K\beta}, \frac{\gamma}{K\beta-2}$, which implies that solutions converge to $|\theta_{qa}| < \frac{\gamma}{K\beta}$ for all points q and a. □

3.5.2 Output Feedback with Noisy Measurements

Now consider the observer dynamics (3.7) and measurement equation (3.8) of a single particle. Analysis of the multi-particle case of output feedback with noisy measurements is the subject of ongoing work. Let $\xi = 0$ and η be bounded measurement noise satisfying $|\eta| < \Gamma$. The estimation error σ denotes the angular difference between θ and $\hat{\theta}$ during the coast phase. Since $\theta, \hat{\theta} \in S^1$, let $\sigma = \theta - \hat{\theta}$ corresponds to the smallest angle between $e^{i\theta}$ and $e^{i\hat{\theta}}$. Since θ is constant during the coast phase, the time derivative of σ in the interval $t_k + \beta$ to $t_k + \beta + \mathcal{T}$ is

$$\dot{\sigma} = -\dot{\hat{\theta}} = -L(\sigma + \eta). \tag{3.65}$$

Consider the quadratic Lyapunov function candidate $U(\sigma) = \frac{1}{2}\sigma^2$. The time-derivative of $U(\sigma)$ along solutions of (3.65) is

$$\dot{U} = -L\sigma^2 - L\eta\sigma. \tag{3.66}$$

The following corollary to Theorem 3.2.2 identifies a bound on σ equal to the sensor-noise bound.

Corollary 3.5.3. *Consider the observer dynamics* (3.7) *with $L > 0$ and bounded sensor noise* $|\eta| < \Gamma$. *The estimation error* $\sigma = \theta - \hat{\theta}$ *converges to* $|\sigma| < \Gamma$.

Proof. Since $|\eta| < \Gamma$, (3.66) becomes

$$\dot{U} \leq -L\sigma^2 + L\Gamma|\sigma|. \tag{3.67}$$

Therefore, U is decreasing outside of the region given by the non-zero roots of (3.67), i.e., $|\sigma| = \pm\Gamma$. □

3.6   Conclusion

The effects of separating sensing and actuation in dynamic systems is not well studied. This chapter presents a bio-inspired dynamic model of planar self-propelled particles with intermittent heading sensing and control. Stability analysis of the noise-free state feedback and output feedback control provides conditions on control and observer gains to ensure local exponential convergence of the equilibrium point in the case of a single particle, multiple particles with synchronous cycles, and multiple particles with asynchronous cycles. The practical stability of the heading estimation and controller is analyzed for bounded measurement and actuator noise, respectively.

Chapter 4: Bioinspired Pursuit in a Structured Environment

4.1 Introduction

I introduce a pursuit-evasion game with a single pursuer and a single evader moving at a constant speed in a still fluid to study how bioinspired predation strategies affect the interaction. In an effort to study the effects of a complex environment on predation, the game occurs in a planar convex environment. Using the expected work required to capture the evader as an objective function I show that minimizing the evader's escape routes can outweigh the effect of incurring additional drag. With this metric, I determine the regions in the bounded environment where it is advantageous for the pursuer to expand its appendages in the active orientation. Similarly, I show that the presence of a boundary positively affects the pursuer by expanding this active orientation shape-changing region in certain directions.

This chapter is organized as follows. Section 4.2 describes the problem formulation, equations of motion, the evader's avoidance and escape regions, and the evader's escape heading probability density function. Section 4.3 presents the expected work required to capture the evader, discusses when the pursuer should prioritize trapping the evader over minimizing the work to capture, and provides qualitative assessment on the optimal pursuit trajectories. Section 4.4 summarizes the results and describes ongoing work.

4.2 Problem Formulation

This chapter considers a pursuit-evasion game with a single pursuer P and evader E in a planar convex environment. The pursuer is modeled as a streamlined rigid body with symmetric movable appendages and its objective is to capture the evader using pure pursuit. The evader is modeled as a self-propelled particle and employs the protean strategy in an effort to avoid capture. Capture is defined as the coincidence of the frontmost point on the pursuer's body and evader.

During pursuit, the pursuer orients its appendages to minimize the evader's escape directions; however, expanding the appendages increases drag. I explore the trade-off between minimizing the work to capture the evader and minimizing the evader's escape directions by using the expected work to capture as the cost function.

The following subsections present the planar interaction model between a pursuer P and an evader E in a bounded environment. First, I derive the equations of motion for the pursuer and evader. Second, I introduce the evader's avoidance and escape regions that are used to derive the probability density function of the evader's escape heading. Third, I derive the probability density function for the evader's escape heading.

4.2.1 Predator-Prey Equations of Motion and Interaction Model

Let the pursuer's body length, width, and appendage length be l_P, w_P, and l_f, respectively. The pursuer's center of mass is positioned at $r_P = x_P + jy_P$ and the body's frontmost point is

$$r_{Pf} = r_P + \frac{l_P}{4}e^{j\theta_P},$$

(4.1)

54

where θ_P is the pursuer's heading.

Inspired by the predation strategies of lionfish [10, 25, 31], the pursuer uses its appendages to minimize the evader's escape routes, but doing so affects the pursuer's size and surface area. Let ψ be the appendage orientation with respect to θ_P. Since the appendages are symmetric, ψ is the orientation of the right appendage and $-\psi$ is the orientation of the left appendage. The endpoints of the left and right appendages are positioned at r_{AL} and r_{AR}, respectively, where

$$r_{AL} \;=\; r_P + \frac{1}{2} w_P j e^{j\theta_P} + l_f e^{j(\theta_P - \psi)} \tag{4.2}$$

$$r_{AR} \;=\; r_P - \frac{1}{2} w_P j e^{j\theta_p} + l_f e^{j(\theta_P + \psi)}. \tag{4.3}$$

When $\psi = 0$, the appendages are held parallel to the line-of-sight vector and the pursuer is in its narrowest configuration, and when $\psi = \pi/2$ the appendages are perpendicular to the line-of-sight vector and the pursuer is in its widest configuration. For simplicity, let ψ be treated as a switching parameter with values of either $\psi = 0$ or $\psi = \pi/2$. Increasing the frontal area of the pursuer comes at the cost of additional drag, where drag is modeled as

$$D_p = b\left(1 + H\sin(\psi)\right) s_P, \tag{4.4}$$

where $b > 0$ is the nominal drag coefficient and $H > 0$ is the percent drag increase due to the orientation of the appendages. I use (4.4) in Section 4.3 to compute the work and expected work to capture the evader as a function of ψ.

To model the planar locomotion of the pursuer, I model a thrust force T_P, linear drag

force D_P, and turning rate u_P. u_P directly controls rate of change of the the pursuer's direction of motion. The body is aligned with this direction. Also assume that the pursuer has a constant speed s_P, i.e., the thrust and drag forces cancel. The equations of motion of P are

$$\dot{r}_P = s_P e^{j\theta_P} \tag{4.5}$$

$$\dot{\theta}_P = u_P. \tag{4.6}$$

Using the pure pursuit strategy, the pursuer seeks to align its heading with the line-of-sight vector such that

$$u_P = K_P \sin(\alpha - \theta_P), \tag{4.7}$$

where α is (2.7) and $K_P > 0$ is a steering control gain.

The evader, on the other hand, is modeled as a point mass self-propelled particle E with intermittent steering. The intermittent steering is divided into an active steering phase during which the evader changes its heading over a duration of β seconds and a non-steering phase during which the evader has a constant heading over a duration of $\mathcal{T}$ seconds. Let the evader's constant speed be denoted as s_E and its heading be θ_E. Adapting the planar intermittent locomotion model from [23], the equations of motion of E are shown in Figure 4.1. Assume β is much smaller than $\mathcal{T}$. The completion of a single active steering phase and single non-steering phase is called a cycle, where k is the cycle number [23].

Using the protean evasion strategy, the evader steers to a random escape heading θ_d during the active steering phase and continues to travel along θ_d during the non-steering
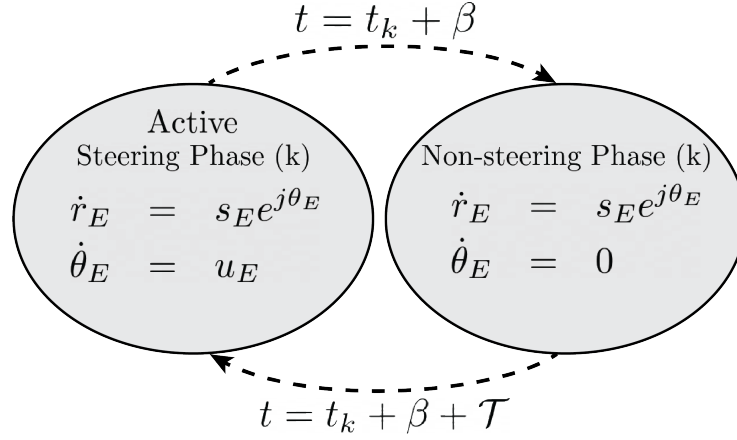
Figure 4.1: Evader intermittent dynamics split into active steering and non-steering phases. β is the time duration of active steering, $\mathcal{T}$ is the non-steering duration, t is the current time, and t_k is the time when the kth active steering phase started.

phase. Let $u_E = K_E \sin(\theta_d - \theta_E)$ be the steering control input, where $K_E > 0$ is a control gain, and the closed-loop heading dynamics during the active steering phase are

$$\dot{\theta}_E = K_E \sin(\theta_d - \theta_E). \tag{4.8}$$
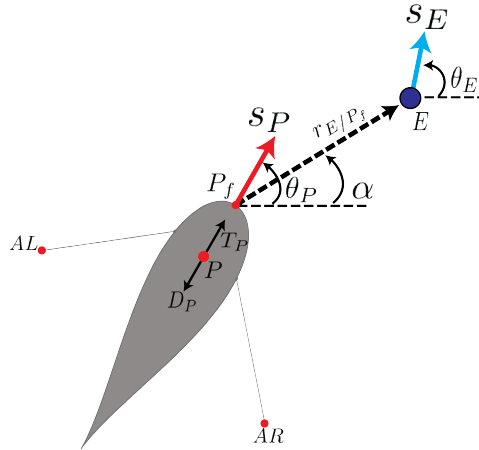
Figure 4.2: Illustration of the free-body diagram of the pursuer and the interaction of the kinematics with the evader.

Figure 4.2 illustrates the pursuer-evader interaction model.

The pursuit and evasion trajectories are governed by the closed-loop dynamics of the pursuer and the evader. Figure 4.3 illustrates the pursuer's pure-pursuit strategy and the evader's protean strategy in a bounded environment shown by solid black lines. In Figure 4.3a, both the pursuer and evader are in their initial configuration where the pursuer has its appendages retracted and is not sensed by the evader. The evader has a limited sensing range with maximum radius R, here arbitrarily set to 1 m, shown as the lightly shaded blue region in Figure 4.3. Let $\mathcal{R}_\mathcal{S} \in \mathbb{R}^2$ be the set of points within the evader's sensing range. If the pursuer or the boundary is outside of $\mathcal{R}_\mathcal{S}$ then the evader does not respond to their presence. However, if the pursuer or boundary are inside of $\mathcal{R}_\mathcal{S}$, then the evader responds by steering away from them in a random direction θ_d according to its probability density function.

At the start of the simulation, the evader enters its active steering phase during which it randomly selects a desired heading θ_d. The next snapshot in Figure 4.3b shows the pursuer entering the evader's sensing region and expanding its appendages. The evader senses the pursuer while in its non-steering phase, so it continues to move in the θ_d direction until the next cycle. In Figure 4.3c, the evader has entered the next cycle during which a new θ_d is randomly selected to avoid the pursuer by steering in the opposite direction. The pursuer keeps its appendages expanded to minimize the evader's escape routes. Lastly, in Figure 4.3d, the evader again steers in a random direction to avoid the pursuer, however, the pursuer captures the evader during the non-steering phase. The simulation parameter values for the pursuer and the evader are shown in Table 4.1. The size of the pursuer's body length, body width, and appendage length were adapted from [84].

(a) time: 0 sec

(b) time: 0.6350 sec

(c) time: 1.2750 sec

(d) time: 1.9050 sec
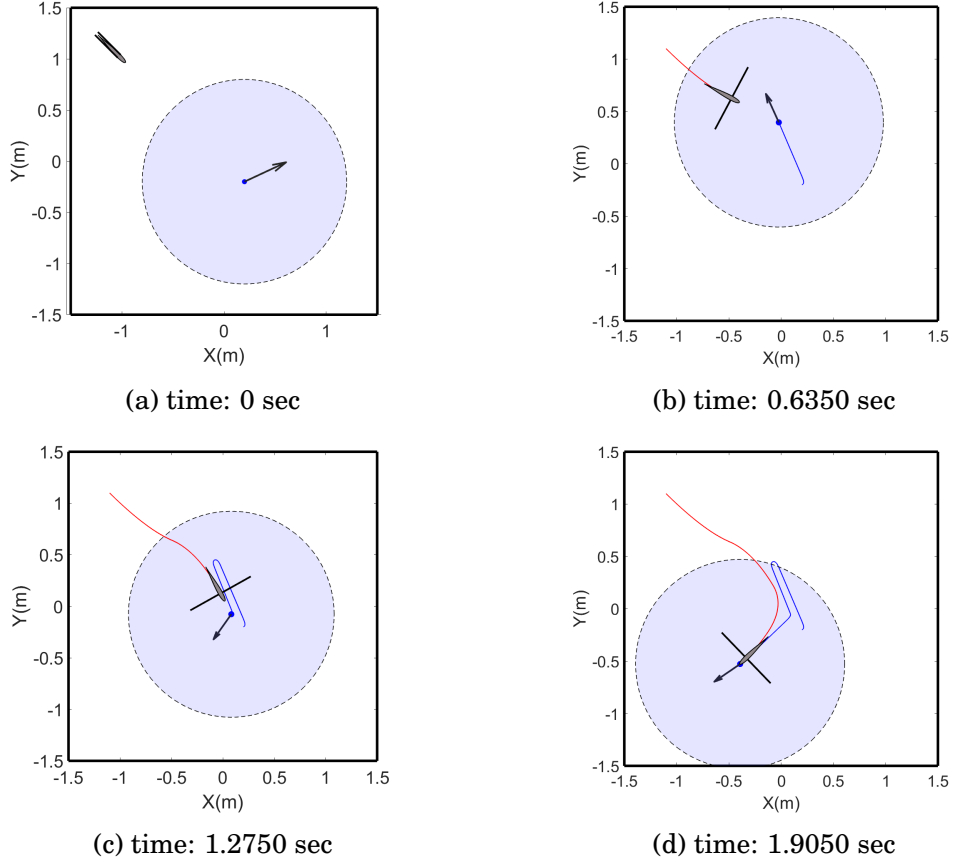
Figure 4.3: Pure pursuit and protean evasion trajectories in a bounded environment at intervals of 0.6350 sec, showing (a) the initial configuration where the blue dot and black arrow is the evader and its velocity orientation, the large blue circle is the evader's sensing region; and (b-d) the trajectories of the pursuer (red line) and evader (blue line) until capture is achieved.

4.2.2 The Evader's Avoidance and Escape Regions

The goal of the evader is to avoid capture from the pursuer and avoid collisions with the boundary $\mathcal{B} \in \mathbb{R}^2$. Due to the limited sensing range, the evader can only respond to these obstacles when they are in its sensing region $\mathcal{R}_{\mathcal{S}}$.

When the pursuer is within the sensing range, the evader detects its relative direction and size. Let $r_{E/AL}$ and $r_{E/AR}$ be the relative positions of the pursuer's left and right

Parameter	Symbol	Value
Pursuer Speed	s_P	1.05 m/s
Pursuer Steering Gain	K_P	50 rad/s
Pursuer Appendage Length	l_f	316×10^{-3} m
Pursuer Body Length	l_P	378×10^{-3} m
Pursuer Body Width	w_P	44.8×10^{-3} m
Evader Sensing Range	R	1.0 m
Evader Steering Gain	K_E	50 rad/s
Evader Speed	s_E	1.0 m/s
Evader Burst Duration	β	0.25 s
Evader Coast Duration	$\mathcal{T}$	2.75 s
Environment Bounds	$\mathcal{B}$	$\{\mathcal{B} \in \mathcal{R}^2 \mid |x| \leq 1.5\text{m}, \ |y| \leq 1.5\text{m}\}$

Table 4.1: Parameter values for the pursuer and evader for simulations

appendages with respect to the evader, respectively, i.e.,

$$r_{E/AL}(\psi) \quad = \quad (r_E - r_P) - \frac{1}{2} w_P j e^{j\theta_P} - l_f e^{j(\theta_P - \psi)} \tag{4.9}$$

$$r_{E/AR}(\psi) \quad = \quad (r_E - r_P) + \frac{1}{2} w_P j e^{j\theta_p} - l_f e^{j(\theta_P + \psi)}. \tag{4.10}$$

The corresponding relative directions of the left and right appendages are

$$\theta_{AL}(\psi) \quad = \quad \arg(r_{E/AL}(\psi)) \tag{4.11}$$

$$\theta_{AR}(\psi) \quad = \quad \arg(r_{E/AR}(\psi)), \tag{4.12}$$

respectively, and the perceived size of the pursuer is the smallest counter-clockwise arc

length δ_P between θ_{AL} and θ_{AR} projected onto the evader's maximum sensing radius, i.e.,

$$\delta_P(\psi) = R\left(\arg\left(e^{j(\theta_{AL}(\psi)-\theta_{AR}(\psi))}\right)\right). \tag{4.13}$$

Note that $\delta_P(\psi) \geq 0$ is the counter-clockwise arc length and has its maximum value when the appendages are fully expanded.

Similarly, when the boundary is within its sensing range, the evader detects the relative direction and angular displacement. Let $\theta_{\mathcal{B}_i}$ and $\theta_{\mathcal{B}_{i+1}}$ be the angles of the ith intersection between the sensible region and the boundary, and let $\delta_{\mathcal{B}_i} \geq 0$ be the smallest counter-clockwise arc length between $\theta_{\mathcal{B}_i}$ and $\theta_{\mathcal{B}_{i+1}}$ projected onto the evader's maximum sensing radius, i.e.,

$$\delta_{\mathcal{B}_i} = R\left(\arg\left(e^{j\left(\theta_{\mathcal{B}_i}-\theta_{\mathcal{B}_{i+1}}\right)}\right)\right). \tag{4.14}$$

To avoid capture, the evader avoids all directions between θ_{AL} and θ_{AR} along arc length δ_P and, to avoid collisions, the evader avoids all directions between $\theta_{\mathcal{B}_i}$ and $\theta_{\mathcal{B}_{i+1}}$ along arc length $\delta_{\mathcal{B}_i}$. I now introduce the concept of an avoidance region $\mathcal{A} \subset \mathcal{R}_{\mathcal{S}}$, defined as any intersection of the sensing region and the boundary and any intersection of the sensing region and the pursuer. Let there be a single avoidance region per set of intersections such that there are $N \geq 0$ avoidance regions in total. Let $\boldsymbol{\phi}_{\mathcal{A}}(\psi)$ be a matrix containing each set
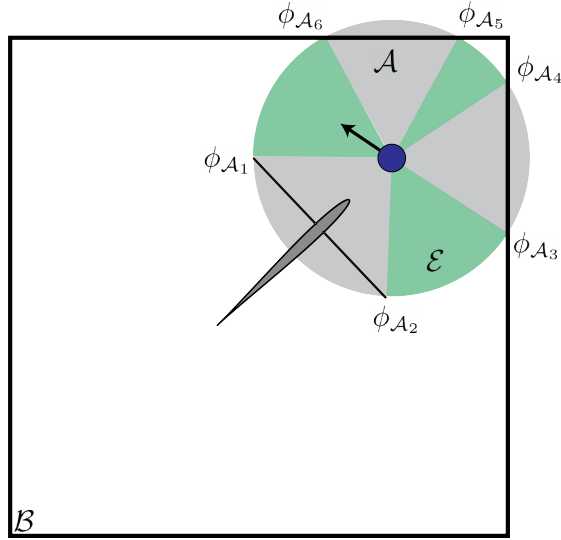
Figure 4.4: Illustration of the evaders sensing region divided into avoidance regions and escape regions. The gray avoidance regions are defined by the intersection angles between the sensing region, the pursuer's appendages, and the boundary (black lines). The green escape regions are the spaces where the evader's possible escape routes exist.

of avoided directions, where

$$
\boldsymbol{\phi}_{\mathcal{A}}(\psi) =
\begin{bmatrix}
\theta_{AL}(\psi) & , & \theta_{AR}(\psi) \\
\theta_{\mathcal{B}_1} & , & \theta_{\mathcal{B}_2} \\
& \vdots & \\
\theta_{\mathcal{B}_N} & , & \theta_{\mathcal{B}_{N+1}}
\end{bmatrix}
=
\begin{bmatrix}
\phi_{\mathcal{A}_1} & , & \phi_{\mathcal{A}_2} \\
\phi_{\mathcal{A}_3} & , & \phi_{\mathcal{A}_4} \\
& \vdots & \\
\phi_{\mathcal{A}_N} & , & \phi_{\mathcal{A}_{N+1}}
\end{bmatrix},
\tag{4.15}
$$

and let $\phi_{\mathcal{A}_n}$ and $\phi_{\mathcal{A}_{n+1}}$ be the intersection angles for the nth avoidance region.

I define the evader's escape region $\mathcal{E} \subset \mathcal{R}_{\mathcal{S}}$ as the compliment of $\mathcal{A}$, as shown in Figure 4.4; let there be $M \geq 1$ escape regions. Let $\boldsymbol{\phi}_{\mathcal{E}}(\psi)$ be a matrix containing each set of

escape directions where

$$\boldsymbol{\phi}_{\mathcal{E}}(\psi) = \begin{bmatrix} \phi_{\mathcal{A}_2} & , & \phi_{\mathcal{A}_3} \\ \phi_{\mathcal{A}_4} & , & \phi_{\mathcal{A}_5} \\ & \vdots & \\ \phi_{\mathcal{A}_{N+1}} & , & \phi_{\mathcal{A}_1} \end{bmatrix} = \begin{bmatrix} \phi_{\mathcal{E}_1} & , & \phi_{\mathcal{E}_2} \\ \phi_{\mathcal{E}_3} & , & \phi_{\mathcal{E}_4} \\ & \vdots & \\ \phi_{\mathcal{E}_M} & , & \phi_{\mathcal{E}_{M+1}} \end{bmatrix}, \tag{4.16}$$

and let $\phi_{\mathcal{E}_m}$ and $\phi_{\mathcal{E}_{m+1}}$ be the intersection angles for the mth escape region. The size of the mth escape region is

$$\delta_{\mathcal{E}_m}(\psi) = \begin{cases} R\left(2\pi - \arg\left(e^{j\left(\phi_{\mathcal{E}_m} - \theta_{\mathcal{E}_{m+1}}\right)}\right)\right), & \text{ccw arc length} > \pi \\ R\left(\arg\left(e^{j\left(\phi_{\mathcal{E}_m} - \theta_{\mathcal{E}_{m+1}}\right)}\right)\right), & \text{otherwise.} \end{cases} \tag{4.17}$$

Note that $\delta_{\mathcal{E}_m}$ and $\boldsymbol{\phi}_{\mathcal{E}}$ are also implicitly dependent on the relative distance between the pursuer and evader.

If there are $N = 0$ avoidance regions, then $\boldsymbol{\phi}_{\mathcal{A}}$ is a null matrix and there are $M = 1$ escape regions, where $\boldsymbol{\phi}_{\mathcal{E}} = [0, 2\pi]$. When there are $N \geq 1$ avoidance regions, there are $M = N$ escape regions. I use (4.16) and (4.17) to compute the probability density function for the evader's protean strategy and to compute the expected work required for the pursuer to capture the evader in Section 4.3.

4.2.3   Probability Density Function of the Evader's Heading

This section defines the evader's probability density function for the random escape heading θ_d. During the active steering phase, the evader steers to θ_d to avoid capture from

the pursuer and to avoid collisions with the boundary. The probability density function for θ_d is dependent on the number of escape regions M and the arc length of each individual escape region $\delta_{\mathcal{E}_m}$.

When there are $N = 0$ avoidance regions and $M = 1$ escape regions, the evader chooses θ_d with a uniform probability density such that $0 \le \theta_d \le 2\pi$. The corresponding probability density function for the $N = 0$ case is

$$f(\theta_d) = \begin{cases} \frac{1}{2\pi}, & 0 \le \theta_d \le 2\pi \\ \\ 0, & \text{otherwise.} \end{cases} \tag{4.18}$$

For the general $N = M \ge 1$ case, let $\phi_{\mathcal{E}_n}$ and $\phi_{\mathcal{E}_{n+1}}$ be the pair of headings for the nth escape region and let $\delta_{\mathcal{E}_n}$ be the corresponding arc length. The probability density function for θ_d is

$$f(\theta_d) = \begin{cases} \dfrac{\delta_{\mathcal{E}_1}}{\sum_{m=1}^{N} \delta_{\mathcal{E}_m}^2}, & \phi_{\mathcal{E}_2} - \delta_{\mathcal{E}_1}/R < \theta_d < \phi_{\mathcal{E}_2} \\ \\ \vdots & \\ \\ \dfrac{\delta_{\mathcal{E}_N}}{\sum_{m=1}^{N} \delta_{\mathcal{E}_m}^2}, & \phi_{\mathcal{E}_{N+1}} - \delta_{\mathcal{E}_N}/R < \theta_d < \phi_{\mathcal{E}_{N+1}} \\ \\ 0, & \text{otherwise.} \end{cases} \tag{4.19}$$

Figure 4.5 illustrates the evader's probability density function for θ_d. The positions of the pursuer and evader are shown in Figure 4.5a, where the evader is also near two boundaries. The corresponding probability density function θ_d is computed using (4.19) and is shown in Figure 4.5b.

In the next section, I use (4.19) to compute the expected work to capture the evader
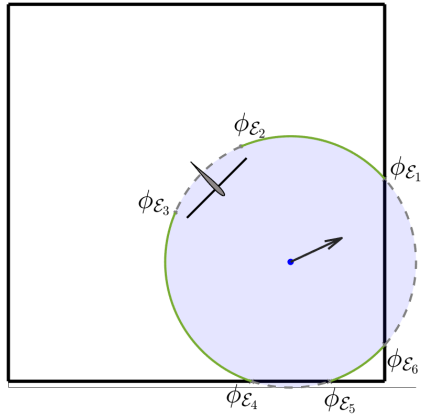
(a) Pursuer evader configuration
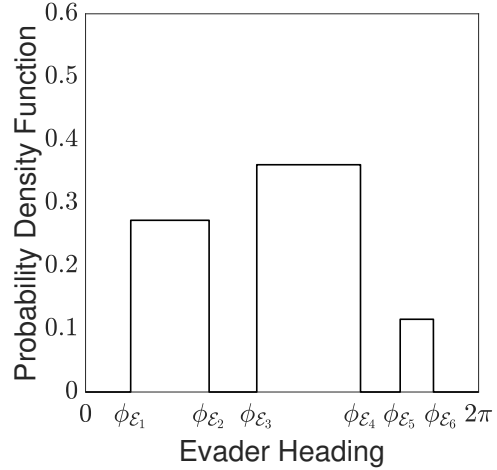
(b) Probability density function of the evader's escape direction

Figure 4.5: Probability density function of the evader's escape direction as a function of the relative position with the pursuer and proximity to the boundary (black lines). (a) the pursuer and the boundary are in the evader's blue sensing region, the solid green lines represent the evader's possible escape directions, and the dashed gray lines represent the evader's avoidance directions; (b) the corresponding probability density function for the evader's escape heading.

for the resting appendages case, $\psi = 0$, and for the active appendages case, $\psi = \pi/2$. I can determine when it is advantageous for the pursuer to expand its appendages by comparing the expected work for these two cases.

4.3   Shape-Changing Predation Strategy

This section analyzes the use of the pursuer's appendages to aid in capturing the evader. First, I compute the work required for the pursuer to capture the evader as a function of the appendage orientation ψ. Second, I derive the expected work to capture the evader using the evader's probability density function for its escape heading. Third, I compare the expected work for the $\psi = 0$ and $\psi = \pi/2$ cases to determine when the efforts to trap the evader outweighs the additional effort due to increased drag.

4.3.1 Work to Capture the Evader and the Expected Work

Since the pursuer has a constant speed s_P, its thrust and drag forces are balanced, such that $T_P = D_p$ and T_P is aligned with the pursuer's velocity s_P. Substituting (4.4) into (2.10) gives the work required to capture the evader during its non-active steering phase, where

$$W_P(\psi) = b\left(1 + H\sin(\psi)\right)s_P|r_{E/P_f}|\left(\frac{K^2 + K\cos(\alpha - \theta_e)}{K^2 - 1}\right).$$
(4.20)

The work to capture the evader depends on the evader's heading θ_e and the pursuer's appendage orientation ψ. Regardless of the evader's heading, the work for $\psi = 0$ is always less than the work for $\psi = \pi/2$ for all $H > 0$, where H is the drag increase due to appendage expansion. Computing the work alone does not account for the minimization of the evader's escape routes by expanding the appendages, so instead I use the expected work.

Due to the stochastic nature of the evader's heading, I compute the expected value of work by substituting (4.20) into (2.12) and evaluate the integral with the appropriate probability density function for the evader's heading.

For the $N = 0$ case, neither the pursuer nor the boundary are in the sensing region and the evader's escape heading probability density function is (4.18). The corresponding expected work is

$$E[W_P(\psi)] = \frac{b\left(1 + H\sin(\psi)\right)s_P|r_{E/P_f}|}{K^2 - 1}K^2.$$
(4.21)

Since the pursuer is beyond the sensing region, (4.21) does not depend on the minimization of escape routes, and the expected work for $\psi = 0$ is always less than the expected work for $\psi = \pi/2$, i.e., $E[W_p(\psi = 0)] < E[W_P(\psi = \pi/2)]$ for $N = 0$. Therefore, when there are no

avoidance regions and when $|r_{E/P_f}| > R$ it is never advantageous for the pursuer to expand the appendages.

For the general $N \geq 1$ case the evader's probability density function for its escape heading is (4.19) and the expected work is

$$E[W_P(\psi)] = \frac{b\left(1 + H\sin(\psi)\right)s_P|r_{E/P_f}|}{(K^2 - 1)\sum_{m=1}^{N}\delta_{\mathcal{E}_m}^2(\psi)}\sum_{q=1}^{N}\delta_{\mathcal{E}_q}(\psi)\left(K^2\frac{\delta_{\mathcal{E}_q}(\psi)}{R} + K\left(\sin\phi_{\mathcal{E}_{2q}} - \sin\left(\phi_{\mathcal{E}_{2q}} - \frac{\delta_{\mathcal{E}_q}(\psi)}{R}\right)\right)\right).$$

(4.22)

Unlike the actual work in (4.20), the expected work in (4.22) accounts for the reduction in the evader's escape region due to the boundary and the orientation of the pursuer's appendages.

4.3.2   Minimizing the Expected Work

This section uses the expected work in (4.22) to analyze the trade-off between minimizing the evader's escape region and minimizing the work to capture. In general the advantages from expanding the appendages depends on the additional drag H felt by the pursuer. To analyze this trade-off I evaluate the conditions on H that satisfy

$$E[W_P(\psi = \pi/2)] \quad \leq \quad E[W_P(\psi = 0)].$$

(4.23)

Condition (4.23) is satisfied if the expected work to capture the evader with expanded appendages is less than or equal to the expected work with appendages at rest.

To simplify the notation, let the summation in (4.22) be represented as

$$X(\psi) = \sum_{q=1}^{N} \delta_{\mathcal{E}_q}(\psi) \left(K^2 \frac{\delta_{\mathcal{E}_q}(\psi)}{R} + K \left(\sin \phi_{\mathcal{E}_{2q}} - \sin \left(\phi_{\mathcal{E}_{2q}} - \frac{\delta_{\mathcal{E}_q}(\psi)}{R} \right) \right) \right),$$ (4.24)

such that the expected work for the $N \geq 1$ case is

$$E[W_P(\psi)] = \frac{b \left(1 + H \sin(\psi) \right) s_P |r_{E/P_f}|}{\left(K^2 - 1 \right) \sum_{m=1}^{N} \delta_{\mathcal{E}_m}^2(\psi)} X(\psi).$$ (4.25)

Substituting (4.25) into (4.23) yields the following condition on H:

$$H \leq \left(\frac{X(0)}{X(\pi/2)} \sum_{m=1}^{N} \frac{\delta_{\mathcal{E}_m}^2(\pi/2)}{\delta_{\mathcal{E}_m}^2(0)} \right) - 1.$$ (4.26)

This condition on H acts as an upper limit to the amount of additional drag due to appendage expansion where condition (4.23) is also satisfied.

During pursuit, if the pursuer's additional drag $H > 0$ satisfies the condition in (4.26), then the minimization of the evader's escape region outweighs the minimization of the pursuer's work to capture, and the pursuer should expand its appendages. For practical systems, the exact value of H depends on the geometry of the pursuer's body.

The remainder of this chapter discusses how conditions (4.23) and (4.26) affect the predation strategy of the pursuer.

4.3.3 The Optimal Shape-Changing Boundary

This section numerically analyzes the spaces where conditions (4.23) and (4.26) are satisfied in the bounded environment. To illustrate the spaces where it is advantageous for the pursuer to extend the appendages, I place the evader in a fixed location and evaluate condition (4.23) for varying positions of the pursuer. The boundary of the area under which conditions (4.23) and (4.26) are satisfied is called the shape-changing boundary. During pursuit, if the pursuer crosses the shape-changing boundary, then it should extend its appendages to minimize the evader's escape directions; otherwise, it should relax its appendages to minimize drag. The size, configuration, and symmetry of the shape-changing boundary depends on the evader's proximity to the domain boundary.

The size of the shape-changing boundary also depends on the additional drag felt by the pursuer. In Figure 4.6, I numerically compute the outer limits of the shape-changing boundary for the predation trajectories shown in Figure 4.3, and I set the additional drag to be $H = 0.15$. As shown in Figure 4.6a, when the evader is far from the boundary $\mathcal{B}$, the shape-changing boundary has axial symmetry with a radius less than the evader's max sensing radius R. Due to the evader's inability to respond when the pursuer is beyond the sensing range, the radius of the shape-changing boundary is always less than or equal to the sensing radius.

Once the pursuer crosses the outer limits of the shape-changing boundary, it is advantageous to expand its appendages, to minimize the evader's escape directions, shown in Figure 4.6b. The shape-changing boundary loses axial symmetry when the evader detects the boundary $\mathcal{B}$; see Figure 4.6c. When the evader is close to a single wall, the radius of the

(a) Time: 0 sec   (b) Time: 1.2750 sec   (c) Time: 1.9050 sec
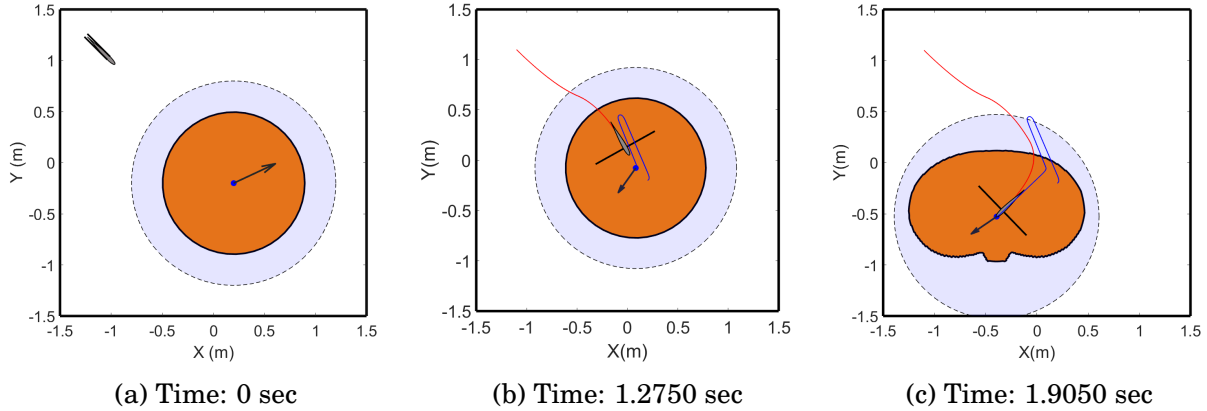
Figure 4.6: Numerical illustrations of the outer limits of the shape-changing boundary (orange region) during pursuit with a 15% increase in drag when the pursuer expands its appendages: (a) the evader (blue dot) is far from the boundary so the shape-changing boundary has axial symmetry; (b) the pursuer enters the evader's sensing region (blue circle) and the shape-changing boundary so it expands it appendages to minimize the evader's escape directions; (c) the evader is near the domain boundary so the shape-changing boundary loses axial symmetry, and the evader is also captured.

shape-changing boundary decrease in directions perpendicular to the wall and increases in directions parallel to the wall. Due to these shorter radial distances, the pursuer needs to get closer to the evader before it is advantageous to expand its appendages; this also implies that approaching the evader in some directions are sub-optimal. The expansion of the radial distance of the shape-changing boundary in other directions implies that, when the evader is near the domain boundary there are optimal pursuit trajectories.

While the figures in Figure 4.6 only illustrate the outer limits of the shape-changing boundary, the figures in Figure 4.7 illustrate the level curves of the percent difference in the expected work to capture the evader due to extending the appendages. The percent difference in expected work is computed by evaluating $E[W_P(\pi/2)]$ and $E[W_P(0)]$, from (4.25), for a fixed evader location and all possible pursuer locations, and using the following for-

mula:

$$\%\text{Diff} = 100\left(\frac{E[W_P(\pi/2)] - E[W_P(0)]}{E[W_P(0)]}\right).$$ (4.27)

Following the gradient of the percent difference level curves yields an optimal pursuit trajectory.

In cases where the evader is far from boundaries, see Figure 4.7a, the level curves maintain axial symmetry with increasing reductions in expected work as $|r_{E/P_f}|$ decreases. The axial symmetry for the level curves implies that there are no sub-optimal pursuit trajectories when the evader is far from boundaries. Optimal pursuit trajectories are more evident when the evader is near a boundary (trajectories are approximately parallel to the detected boundary). Figure 4.7b shows the level curves of the percent difference when the evader is near a single wall. The sub-optimal trajectories are perpendicular to the detected boundary since the distance between the pursuer and the evader must be smaller before extension of the appendages becomes advantageous.

When the evader is near a detected boundary, the optimal pursuit trajectories imply that directly cornering the evader such that it has an equal probability of choosing any escape direction parallel with the boundary is sub-optimal. In cases when the evader is near a single wall or near a corner, the optimal pursuit trajectories minimize the number of escape regions for the evader.

Thus far, the additional drag was assumed to be $H = 0.15$; however, the max allowable additional drag is computed with (4.26) and is a function of the relative distance between the pursuer and the evader. To illustrate how the additional drag affects the shape-changing boundary, I evaluate (4.26) for a fixed evader position and all possible

(a) Time: 1.2750 sec   (b) Time: 1.9050 sec
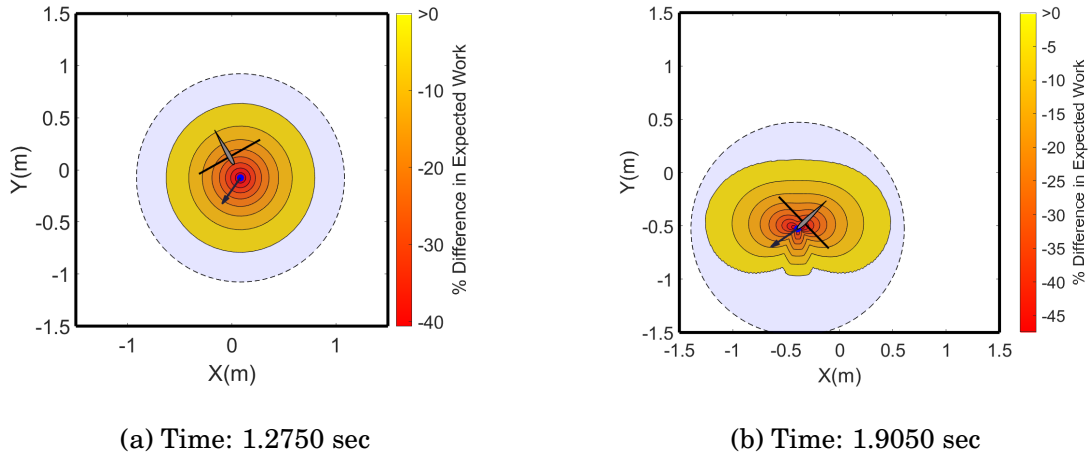
Figure 4.7: Numerically computed level curves for the percent difference in expected work to capture the evader during pursuit and a 15% increase in drag: (a) the evader is far from the domain boundaries and the level curves of the percent difference in expected work have axial symmetry; (b) the evader is near a single wall with optimal pursuit trajectories being approximately parallel to the boundary minimizing the number of the evader's M escape regions.

pursuer positions in the bounded environment. Figures 4.8a and 4.8b show snapshots during pursuit with the level curves of the maximum additional drag that satisfies (4.23). The level curve of the additional drag for $H = 0.15$ is equivalent to the outer limit of the shape-changing boundary in Figure 4.6. As the value of H increases the radius of the shape-changing boundary decreases; implying that for higher values of H, the pursuer needs to get closer to the evader before it is advantageous to minimize the evader's escape directions. While there are benefits for this predation strategy for high values of additional drag, the close proximity requirement makes it less tractable.

4.4   Conclusion

This chapter presents a bioinspired pursuit-evasion game in a closed environment with one pursuer and one evader. I model the pursuer as a streamlined body with sym-
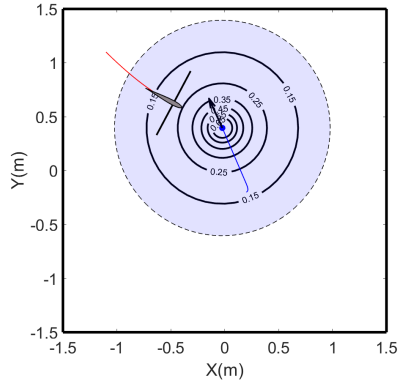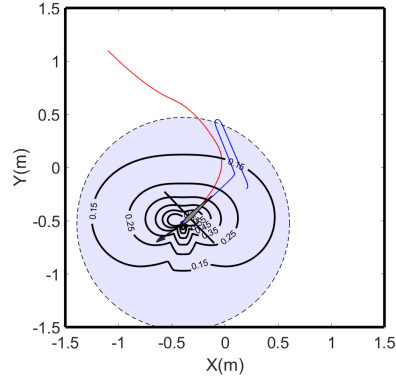
(a) Time: 0.6350 sec   (b) Time: 1.9050 sec

Figure 4.8: Snapshots of the pursuit trajectories with numerical illustrations of the shape-changing boundary for various drag coefficients: (a) as the pursuer approaches the evader and crosses the shape-changing boundary for $H = 0.15$ it expands its appendages to minimize the evader's escape directions; (b) the evader is captured near a detectable wall and the level curves of the shape-changing boundary loses axial symmetry.

metric movable appendages in pure-pursuit of an intermittently steering evader. To avoid capture, the evader uses a protean strategy, which steers in a random escape direction to be less predictable to the pursuer. The evader's random escape direction has a probability density function that depends on its proximity to the pursuer and boundary and the orientation of the pursuer's appendages. The bioinspired predation strategy allows the pursuer to actively use its appendages to minimize the evader's escape routes, but at the cost of additional hydrodynamic drag. I show that actively using the appendages to minimize the evader's escape routes outweighs the effects of additional drag once the pursuer is sufficiently close to the evader. Furthermore, I show that when the evader is far from detectable boundaries, all pursuit trajectories are optimal; whereas, not all trajectories are optimal when the evader is near a boundary. The work in this chapter gives insights to understanding the predation strategies of biological systems and provides a mathematical model that describes when to use this strategy for engineered systems.

Chapter 5:   Planar Formation Control for a School of Robotic Fish Implementation

5.1   Introduction

This chapter investigates planar formations in a novel setting: a system of second-order oscillators with nonlinear dynamics and nonholonomic constraints on the tangent bundle of the N-torus. The closed-loop swimming dynamics of the fish robots are represented by the Chaplygin sleigh [85], [54], a nonholonomic mechanical system driven by an internal reaction wheel. The control design is inspired by prior work on collective motion of self-propelled particles [19, 69, 70, 86]; however, a key distinction is that agents have second-order limit-cycle dynamics with time-varying speed. Thus, novel parallel formations are achieved in an average sense.

My contributions of this chapter are (1) system identification of the reaction-wheel motor dynamics and the design of an optimal estimation and tracking controller that follows the torque commands of the formation control; and (2) experimental validation of the parallel formation control law on a school of bio-inspired robotic fish (see Fig. 1.2). The proposed control algorithms are illustrated through both numerical simulations and experiments in the University of Maryland's Neutral Buoyancy Research Facility.

The remainder of the chapter is organized as follows. Section II provides Chaplygin sleigh dynamics. Section III presents a control design to achieve parallel formations for a robotic fish school. Section IV presents the experimental implementation and results for the parallel formation control for a school of robotic fish. Lastly, Section V summarizes the chapter.

5.2 Robotic Fish Dynamics and Parallel Formation Control

The Chaplygin sleigh is a canonical nonholonomic mechanical system consisting of a rigid body moving in the plane that is supported by two frictionless sliding points and a single knife edge that allows no motion perpendicular to its edge [87]. Previous studies have demonstrated that a fish robot driven by an internal reaction wheel can be modeled as a Chaplygin sleigh due to the nonholonomic constraint imposed by the Kutta condition [85], [54], which constrains the fluid flow at the trailing edge. As the reaction wheel spins back and forth, it flaps the robot's body, which interacts with the surrounding fluid to generate thrust.

(a) Self-propelled particle (b) Reaction-wheel driven robotic fish
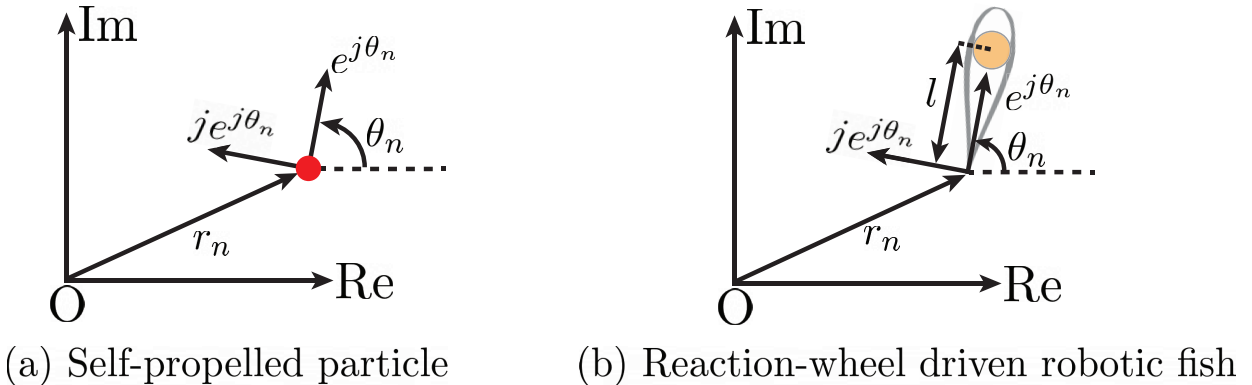
Figure 5.1: Coordinates and unit vectors: (a) the self-propelled particle; (b) the Chaplygin-sleigh model of a robotic fish. In (b), the hydrofoil shape represents the fish robot body and a bronze-colored reaction wheel is shown at the center of mass.

Consider a system of N fish robots each modeled as a Chaplygin sleigh with the following dynamics in state-space form [54]:

$$\dot{r}_n = s_n e^{j\theta_n}$$

$$\dot{\theta}_n = \omega_n$$

$$\dot{s}_n = l\omega_n^2 - bs_n \qquad (5.1)$$

$$\dot{\omega}_n = -\frac{mls_n}{d}\omega_n - \frac{u_n}{d},$$

where $r_n \in \mathbb{C}$ is the position of the trailing edge of the fish robot (see Fig. 5.1b), $s_n \in \mathbb{R}$ is the swimming speed, $\theta_n \in \mathbb{T}$ is the velocity orientation, $\omega_n \in \mathbb{R}$ is the angular rate of the nth fish, and $u_n \in \mathbb{R}$ is the applied torque, where $n = 1, \ldots, N$. Furthermore, $b \geq 0$ is the drag coefficient, and $m > 0$, $l > 0$, and $d > 0$ are the mass, length, and moment of inertia, respectively. Unlike the self-propelled particle (2.3), the speed of the Chaplygin sleigh (5.1) is not constant and the control input is a torque rather than an angular rate.

Prior work has established that the Chaplygin-sleigh model exhibits limit-cycle dynamics under open-loop periodic control inputs [88], as well as feedback control [54] [43]. Consider the feedback control [54]

$$u_n = d(-K_1\omega_n - K_2\sin(\bar{\theta}_n - \theta_n)), \qquad (5.2)$$

where $\bar{\theta}_n$ is the desired heading angle of the nth fish, and $K_1, K_2 > 0$ are feedback gains.

Substituting (5.2) into (5.1) yields the closed-loop system [54]

$$\dot{r}_n = s_n e^{j\theta_n}$$

$$\dot{\theta}_n = \omega_n$$

$$\dot{s}_n = l\omega_n^2 - bs_n$$

$$\dot{\omega}_n = -\frac{ml}{d}s_n\omega_n + K_1\omega_n + K_2\sin(\bar{\theta}_n - \theta_n).$$

(5.3)

The control law (5.2) that enables each fish robot to swim in a desired direction can be modified, with interactions from neighboring fish, to achieve collective motion of the school, as described next.

Consider a collection of N identical fish robots modeled by the Chaplygin sleigh system (5.1). Assume a sufficiently large drag coefficient so that $s_n \to (l/b)\omega_n^2$ and let $a = \frac{ml^2}{bd}$. For the purposes of control design, the simplified Chaplygin sleigh system (5.1) becomes

$$\dot{r}_n = (l/b)\omega_n^2 e^{j\theta_n}$$

$$\dot{\theta}_n = \omega_n$$

$$\dot{\omega}_n = -a\omega_n^3 - \frac{u_n}{d}.$$

(5.4)

Consider the potential

$$V_p(\boldsymbol{\theta}, \boldsymbol{\omega}) = \frac{1}{2}\boldsymbol{\omega}^T\boldsymbol{\omega} + \frac{1}{2N}K_2\langle e^{j\boldsymbol{\theta}}, Le^{j\boldsymbol{\theta}}\rangle.$$

(5.5)

The time-derivative of $V_p(\boldsymbol{\theta})$ is

$$\dot{V}_p(\boldsymbol{\theta}, \boldsymbol{\omega}) = \dot{\boldsymbol{\omega}}^{\mathrm{T}} \boldsymbol{\omega} + \frac{1}{N} K_2 \langle \frac{d}{dt} e^{j\boldsymbol{\theta}}, L e^{j\boldsymbol{\theta}} \rangle, \tag{5.6}$$

where, along trajectories of (5.4),

$$\dot{\boldsymbol{\omega}}^{\mathrm{T}} \boldsymbol{\omega} = \sum_{k=1}^{N} \left(-a\omega_n^3 - d^{-1} u_n \right) \omega_n, \tag{5.7}$$

and

$$\langle \frac{d}{dt} e^{j\boldsymbol{\theta}}, L e^{j\boldsymbol{\theta}} \rangle = \sum_{n=1}^{N} \langle j e^{j\theta_n}, L_n e^{j\boldsymbol{\theta}} \rangle \omega_n. \tag{5.8}$$

By choosing the control

$$\begin{aligned}
u_n &= b(-K_1 \omega_n + \frac{K_2}{N} \langle j e^{j\theta_n}, L_k e^{j\boldsymbol{\theta}} \rangle) \\
&= b(-K_1 \omega_n + \frac{K_2}{N} \sum_{p \in \mathcal{N}_n} \sin(\theta_p - \theta_n)),
\end{aligned} \tag{5.9}$$

and substituting (5.7)–(5.9) into (5.6), $\dot{V}_p(\boldsymbol{\theta}, \boldsymbol{\omega})$ becomes

$$\dot{V}_p(\boldsymbol{\theta}, \boldsymbol{\omega}) = \sum_{n=1}^{N} (-a\omega_n^2 + K_1)\omega_n^2. \tag{5.10}$$

The feedback control law (5.9) relies only on relative-state measurements between agents and does not include feedback linearization of the agents' dynamics. Recall K_1, $K_2 > 0$ are control gains. Since (5.10) is a summation of quartic functions with roots at

Table 5.1: Parameters used to simulate the fish robot system, based on the experimental testbed.

Parameter	Symbol	Value
Mass	m	1.4 kg
Length	l	0.31 m
Drag coefficient	b	0.5
Moment of inertia	d	0.1395 kg·m^2
Control gains	(K_1, K_2, K_3)	$(0.5, 3, 1)$

$\omega_n = 0$ and $|\omega_n| = \sqrt{K_1/a}$, then $\dot{V} < 0$ outside $\Omega_p = \{(\boldsymbol{\theta}, \boldsymbol{\omega}) \in \mathbb{T}^N \times \mathbb{R}^N : |\omega_n| \le \sqrt{K_1/a} \; \forall \; k \in \mathcal{V}\}$.

Therefore, all trajectories are trapped in Ω_p. The gain K_2 in (5.9) is chosen to ensure forward flapping motion for (5.1), as discussed in Section 5.2.

(a) Limit cycle in (v_k, ω_k) plane   (b) Limit cycle in (θ_k, ω_k) plane   (c) Paths of fish robots   (d) Parallel potential, $V_p(t)$
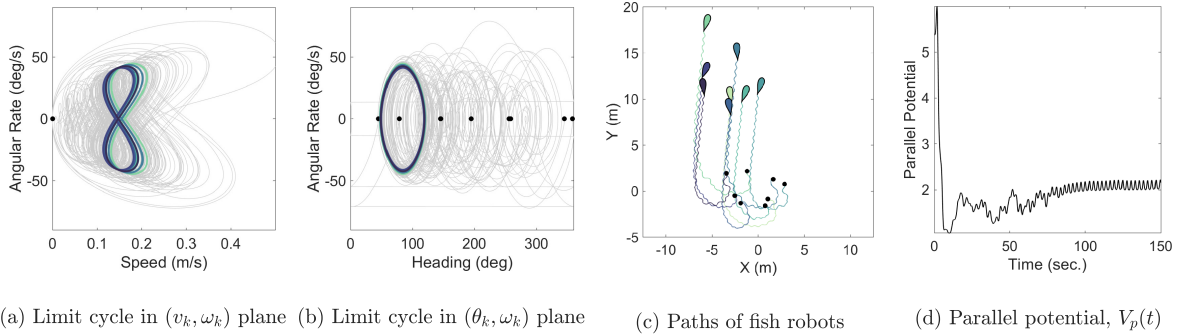
Figure 5.2: Simulation of (5.1) with parallel formation control (5.9) and $N = 8$ identical fish. The black circular markers in (a)–(c) indicate the initial simulation states. The last 10 seconds of the limit cycle in (a) and (b) are shown with colored lines.

The control law (5.9) is illustrated by numerical simulation using control (5.9) and the full dynamics (5.1). The simulation was conducted for 150 seconds with $N = 8$ robots using the parameters listed in Table 5.1. The robots were initialized with random headings and zero linear and angular velocities. A communication range of three meters determined the communication topology, which remained invariant during the simulation based on the agent's random initial positions. Figures 5.2a and 5.2b show all N robots converging to the same limit cycle in the (θ_n, ω_n) and (s_n, ω_n) planes. As a result, all robots move in the

same direction (on average), as shown in Fig. 5.2c. The parallel potential, $V_p(t)$, initially decreases (see Fig. 5.2d), but instead of converging to zero, it oscillates around a fixed value as the robots converge to different phases on the same limit cycle.

5.3   Experimental Testbed

This section describes the implementation of the parallel formation control law (5.9) on a school of robotic fish and experimental results. First, the experimental testbed used in this chapter is briefly described. Next, results from system identification experiments are presented that provide parameters for a model of the reaction wheel dynamics. Based on this model, an inner-loop linear-quadratic-Gaussian (LQG) controller is implemented to track a desired reference torque generated from the formation control law using the onboard motor's angular velocity measurements. Lastly, results from a series of in-water experiments demonstrating the parallel formation control are presented.

The fish-inspired soft robots used in the experiments (see Fig. 1.2) are each driven by a Pololu 12V DC motor (with a 4.4 to 1 gear ratio) that oscillates a reaction wheel located at each robot's center of mass. Each fish robot measures its orientation with an on-board BNO055 inertial measurement unit (IMU) sensor that features a built-in extended Kalman filter. A micro-SD card is used to store sensor data and a 900MHz xBee radio enables each fish robot to communicate with a ground station and other fish robots on the water's surface. Each fish robot performs onboard sensor processing and control with a Teensy 3.2 microcontroller. For a more detailed discussion of the fish robots' design, refer to [54].

The experiments were conducted in a 367,000 gallon water tank at the Neutral Buoyancy Research Facility at the University of Maryland, College Park. An overhead camera is mounted above the experimental area to record the true position of each robotic fish; however, the position data is not used in real time by the fish for formation control. Instead, during formation control experiments, each robot exchanges orientation data from their onboard IMU with other fish in the school using the xBee radios. Since the position of each robotic fish is not computed in real-time, an invariant complete communication graph was used in the experiments; whereas, a proximity-based communication graph was used in simulation. The overhead camera images are post-processed after each experiment to visualize the trajectory of each robotic fish. The image processing uses MATLAB's built-in corner/object detection based on a minimum eigenvalue algorithm [89] and a built-in constant velocity Kalman filter for object tracking. Since all of the sensing and control law computations occur onboard, the school of robotic fish are a self-contained system when performing formation control experiments. The block diagram in Fig. 5.3 gives an overview of the experimental testbed.

5.3.1   System Identification of the Actuator

The nonlinear control law (5.9) generates a reference torque command that steers the fish robots to their respective formations. However, this torque cannot be commanded directly since the control input into the reaction wheel system is the voltage applied to the DC motor generated by the motor driver and Teensy micro-controller. Furthermore, the only available measurement is the angular velocity of the motor's shaft measured by
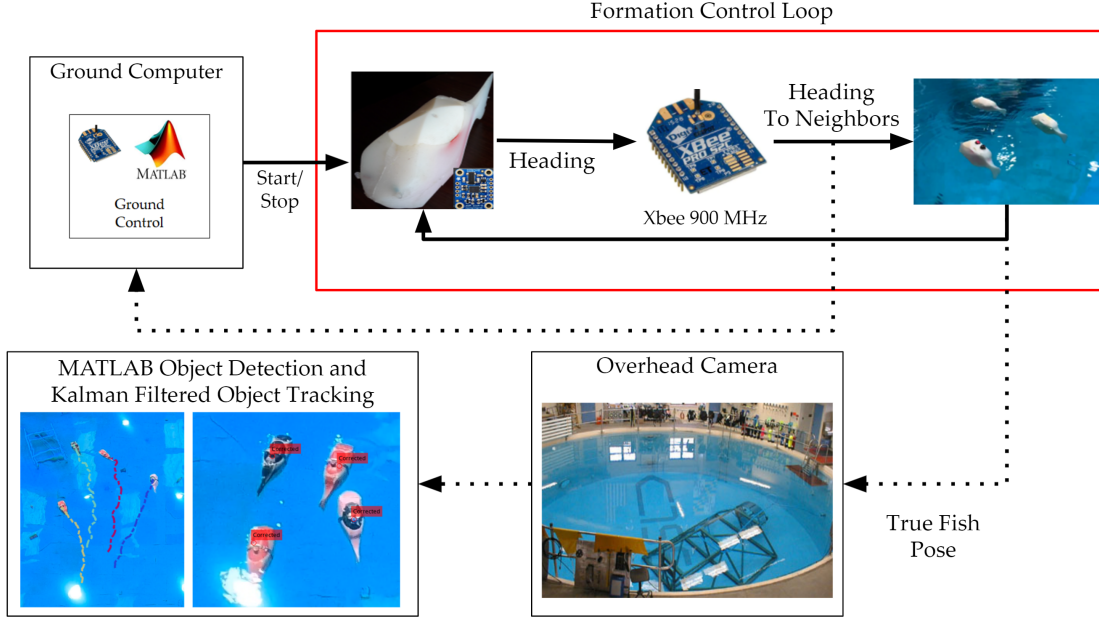
Figure 5.3: Block diagram of the experimental testbed. Since all of the sensing and control law computations occur onboard, the school of robotic fish are a closed self-contained system when performing parallel formation control experiments.

an encoder. Thus, to track the reference torque a linear-quadratic-Gaussian (LQG) controller and estimator was implemented. The LQG controller assumes the following motor dynamics [90]:

$$\Lambda \;=\; \mu\frac{di}{dt} + Ri + e \tag{5.11}$$

$$e \;=\; K_e\dot{\psi} \tag{5.12}$$

$$\tau \;=\; K_\tau i \tag{5.13}$$

$$J\ddot{\psi} \;=\; \tau - \zeta_m\dot{\psi}, \tag{5.14}$$

where Λ is the voltage input, R is the motor's electrical resistance, μ is the inductance, i is the current, e is the motor's back electromotive force (EMF), $\dot{\psi}$ is the angular rate of the output shaft, J is the sum of inertias between the reaction wheel and motor's output

shaft, τ is the torque applied by the motor, ζ_m is the internal damping friction applied to output shaft, and K_e and K_τ are the motor's generator and torque constants, respectively. To identify the values of the DC motor and reaction wheel parameters, a series of system identification experiments were conducted, as described next.

The resistance of the motor R was measured directly with an ohm meter, and the sum of the motor and reaction wheel inertias J was approximated using analytical expressions for the moment of inertia of a cylinder about its axis of symmetry with a known mass and diameter. To determine the motor generator constant K_e, substitute (5.12) into (5.11) and examine the system at steady current state, i.e., $di/dt = 0$. Solving for $\dot{\psi}$ yields

$$\dot{\psi} = \frac{1}{K_e}(\Lambda - Ri).$$ (5.15)

Using a Rigol DP711 power supply and quadrature encoder attached to the motor's output shaft, a series of constant voltages were applied to the motor. For each voltage, the current through the motor and the angular velocity of the output shaft at steady state were recorded. A linear regression was used to determine the quantity $1/K_e$, which is the slope of the line in (5.15) and Fig. 5.4a.

The internal friction coefficient ζ_m was found by setting the torque to zero, i.e., $\tau = 0$ in (5.14), and solving the resulting differential equation to obtain

$$\ln(\dot{\psi}(t)) = -\frac{\zeta_m}{J}t + \ln(\dot{\psi}(0)),$$ (5.16)

where $\dot{\psi}(0)$ is the initial shaft angular velocity. Notice that (5.16) is a linear equation that

describes $\ln(\dot\psi)$ as a function of time. A similar technique as described previously can be used to find $-\zeta_m/J$ from a time-history of torque-free motor data. To identify the damping parameter, the motor was initialized with a constant nonzero angular velocity and the input voltage was removed. The motor's angular velocity was recorded as it decays under internal friction. As before, a linear regression was used to determine the slope $-\zeta_m/J$ in (5.16) from Fig. 5.4b and, hence, ζ_m can be inferred since J is known.

To determine the torque constant K_τ, substitute (5.13) into (5.14) at steady state ($\dot\psi$ constant) and solve for $\dot\psi$ to obtain

$$\dot\psi = \frac{K_\tau}{\zeta_m} i. \tag{5.17}$$

By repeating the procedure used to determine K_e, using the value of ζ_m, the value of K_τ is found from the slope K_τ/ζ_m in (5.17) and Fig. 5.4c.

Since the inductance μ only plays a role in the transient response of the motor, which are sufficiently fast, I estimate this parameter heuristically. The simulated response of the motor to a sinusoidal voltage input is visually compared to the actual response of the motor under the same input. The process is repeated while adjusting the value of μ to obtain a similar response, as shown in Fig. 5.4d.

Lastly, the motor was found to exhibit a range of deadband voltages near zero that resulted in the motor being unresponsive. To determine the range of this deadband, a series of incrementally increasing voltages were applied to the motor, giving an approximate deadband range of ±4V. The parameter values determined through this system identification process are summarized in Table 5.2.

Table 5.2: Motor parameters identified through system identification for the Pololu 12 V DC Motor (with 4.4 to 1 gear ration) and reaction wheel

Parameter	Symbol	Value
Inductance	μ	0.005 H
Generator constant	K_e	0.0506 V·s/rad
Torque constant	K_τ	0.2137 N·m/A
Damping coefficient	ζ_m	-1.1016×10^{-4} N·m·s/rad
Resistance	R	2.5 Ω
Inertia	J	1.7405×10^{-4} kg·m^2
Deadband	-	±4 V

(a) Generator constant   (b) Linear damping   (c) Torque constant   (d) Inductance
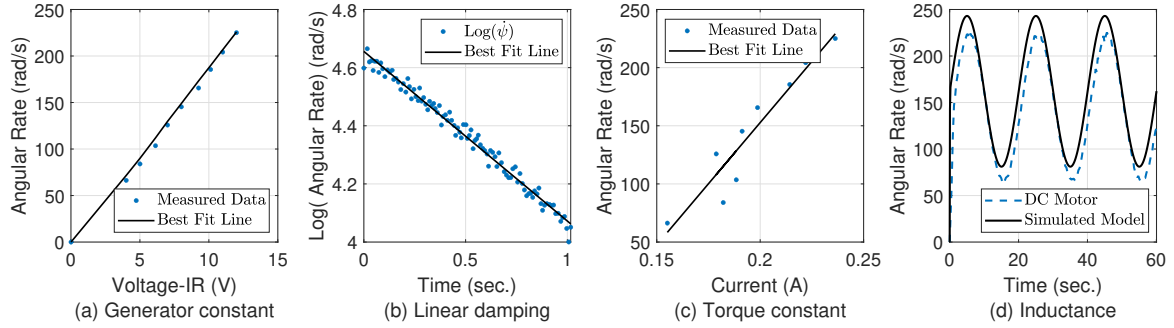
Figure 5.4: Experimental data used to identify motor-reaction wheel dynamics: Panels (a)–(c) are used to infer the values of the generator constant, linear damping, and torque constant through linear regression. Panel (d) compares the motor's simulated and actuated response with a best guessed value of the inductance.

5.3.2 Torque Tracking Controller

To implement the LQG torque controller and state estimator for the DC motor, convert (5.11)–(5.14) into state space form where $\boldsymbol{q} = \begin{bmatrix} \tau, \dot{\psi} \end{bmatrix}^T$ denotes the states of the motor and the output is $\Upsilon = \dot{\psi}$. The continuous-time state space equations take the form

$$\dot{\boldsymbol{q}} = \boldsymbol{A}\boldsymbol{q} + \boldsymbol{B}\Lambda \tag{5.18}$$

$$\Upsilon = \boldsymbol{C}\boldsymbol{q} \tag{5.19}$$

where

$$\boldsymbol{A} = \begin{bmatrix} -\frac{R}{\mu} & -\frac{K_e K_\tau}{\mu} \\ \frac{1}{J} & -\frac{\zeta_m}{J} \end{bmatrix}, \boldsymbol{B} = \begin{bmatrix} \frac{K_\tau}{\mu} \\ 0 \end{bmatrix}, \text{ and } \boldsymbol{C} = \begin{bmatrix} 0 & 1 \end{bmatrix}. \tag{5.20}$$

For implementation onboard the micro-controller, the continuous system (5.18)–(5.19) is converted into a discrete-time system (with an addition of torque process noise and heading measurement noise):

$$\boldsymbol{q}_{k+1} = \boldsymbol{\Phi} \boldsymbol{q}_k + \boldsymbol{\Gamma} \Lambda_k + \boldsymbol{\xi} w_k \tag{5.21}$$

$$\Upsilon_k = \boldsymbol{C} \boldsymbol{q}_k + \eta_k, \tag{5.22}$$

where [91]

$$\boldsymbol{\Phi} = e^{\boldsymbol{A}\Delta t}, \quad \boldsymbol{\Gamma} = \left(\int_0^{\Delta t} e^{\boldsymbol{A}\tau} d\tau \right) \boldsymbol{B}, \quad \boldsymbol{\xi} = \begin{bmatrix} 1 \\ 0 \end{bmatrix}, \tag{5.23}$$

k is an integer indexing the discrete state, $\Delta t = 100 Hz$ is the time-step of the microcontroller, w_k is zero-mean, Gaussian, additive process noise with variance σ_w^2, and η_k is zero-mean, Gaussian, additive measurement noise with variance σ_η^2.

I adopt the standard approach outlined in [91] and [82] to implement a discrete-time Kalman filter for the system (5.21)–(5.22). The estimated state $\hat{\boldsymbol{q}}_k$ is used in a linear-quadratic-regulator (LQR) feedback control law of the form $\Lambda_k = \boldsymbol{\kappa}^T (\boldsymbol{q}_d - \hat{\boldsymbol{q}}_k)$, where the $\boldsymbol{\kappa}$ is a gain matrix found by solving the discrete-time algebraic Riccati equation and $\boldsymbol{q}_d$ are the desired state values.
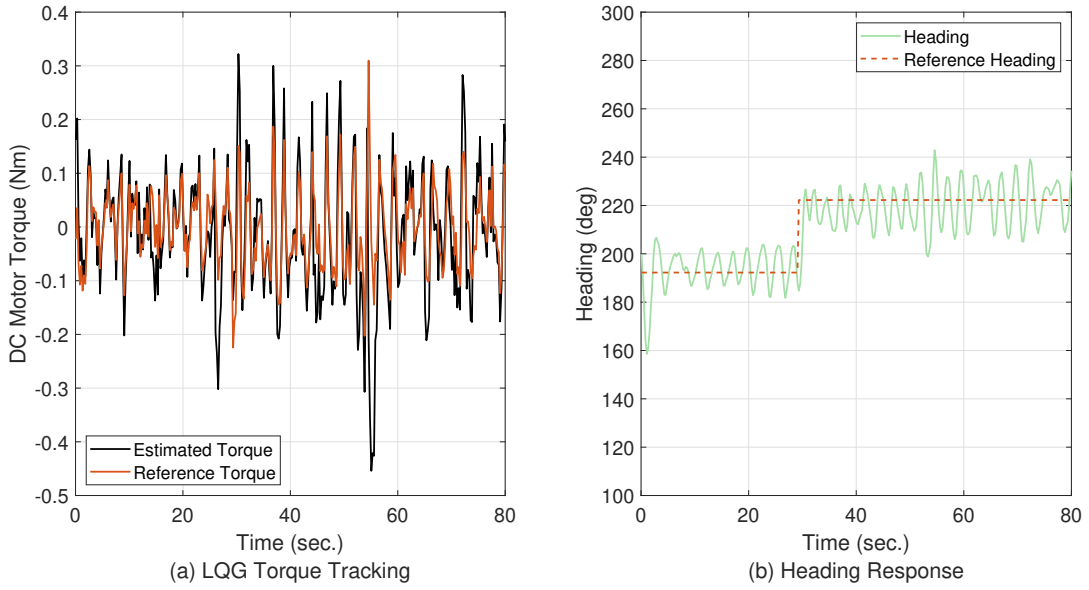
Figure 5.5: Experimental data from a closed loop heading controller (5.2): (a) the reference torque produced by (5.2) and the estimated torque from the LQG controller. (b) fish robot's closed loop heading response to a step input reference heading.

Numerical values used in the LQG controller and estimator design are given in Table 5.3.

To evaluate the LQG torque controller/estimator, the control law (5.2) was used to generate a reference torque for a step input change in desired heading. The performance of the torque tracking controller is shown in Fig. 5.5a, and the heading trajectory of the fish robot during this experiment is examined in the next section.

Table 5.3: Parameters used in a LQG controller and estimator

Parameter	Symbol	Value
Process noise variance	σ_ω^2	$1\ \mathrm{V}^2$
Measurement noise variance	σ_η^2	$0.89\ \mathrm{(rad/s)}^2$
LQR gain	$\boldsymbol{\kappa}$	$[-9.57, 0.24]^T$

5.4 Experimental Results

This section presents the experimental results of two nonlinear steering controllers. First, I experimentally validate the steering controller for a single fish robot where a desired direction is specified by the ground computer. Second, I discuss the experimental results for the nonlinear parallel formation controller for multiple robotic fish.

5.4.1 Single Fish Robot Heading Control

I first examine the accuracy of the closed-loop directional controller (5.2), where θ_d is a desired heading. After testing (5.2) on a single robotic fish, I found that the DC motor's deadband does not allow the average heading to completely converge to θ_d. When the fish robot's heading is close to the desired heading, the voltage required to close the gap is too small and falls within the dead zone making the motor unresponsive. The accuracy of (5.2) is limited on our testbed due to this voltage deadband, but can also be mitigated by choice of the values of the nonlinear control gains K_1 and K_2. In both (5.2) and (5.9), increasing the value of K_2 makes the control laws more sensitive to relative heading errors and increases the torque required to minimize the error. Similarly K_1 amplifies the torque and, therefore the voltage input required to keep the fish swimming. Tuning these control gains increases the accuracy of the aforementioned control laws. The experimental results of this test with a step input for θ_d is shown in Fig. 5.5b. The fish robot's heading oscillates about a desired heading with a small persistent error between the average and desired headings. The control gains used in this experiment are $K_1 = 0.5$ and $K_2 = 7$.
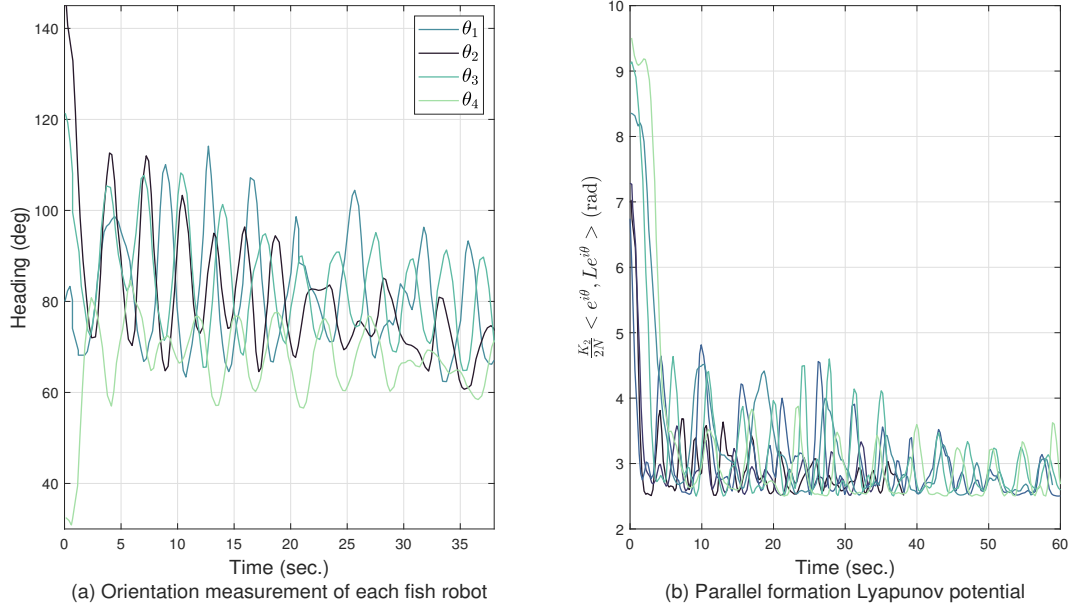
Figure 5.6: Parallel formation control onboard sensor data: (a) orientation measurements from onboard IMU for each fish robot while achieving a parallel formation. (b) experimental parallel formation misalignment potential computed for six independent experiments.

5.4.2 Parallel Formation

To validate the theoretical results of the parallel formation control law (5.9), the results from six experiments are presented. The fish robots' micro-controller uses IMU measurements for the heading and xBee radios for communication within the school. An overhead camera observes the positions of each fish robot; these were not used by the school during the experiments.

Four fish robots were initialized with random initial positions and orientations at the beginning of each parallel formation control experiment (implemented with gains $K_1 = 3$ and $K_2 = 5$). Consensus was achieved by the four fish with a small phase shift (up to 20 degrees) of the mean heading for each fish. This offset may be attributed to excess noise in angular velocity measurements and the aforementioned voltage dead zone. An example

heading time-history from one of the experiments is shown in Fig. 5.6a.

The excess noise in the angular velocity measurements caused large spikes to appear when computing the Lyapunov potential (5.5) from experimental data. Thus, to illustrate the convergence of this potential, the $\frac{1}{2}\boldsymbol{\omega}^T\boldsymbol{\omega}$ term was removed, leaving only the heading alignment term $\frac{K_2}{2N} < e^{j\theta}, Le^{j\theta} >$ plotted in Fig. 5.6b for each of the six experiments. The potential function does not decrease completely to zero when consensus is achieved because each robot converges to a different phase on the limit cycle.

An example trajectory of the fish robots in Fig. 5.7a shows the fish robots achieving consensus and swimming in a parallel formation. However, since the ground truth orientations of the fish robots are not used, errors in the IMU measurements sometimes cause a subset of the school to swim in a different direction than the rest of the school, as shown in Fig. 5.7b. The error in IMU measurements may be caused by an erroneous calibration or magnetic anomalies in the water tank interfering with the onboard magnetometer.

5.5   Conclusion

Nonlinear control laws are proposed that stabilize parallel and circular formations in a model of N planar fish robots. The control design approach extends prior work on collective motion of self-propelled particles to a school of robotic fish with Chaplygin sleigh dynamics. The feedback control laws rely only on relative-state measurements between agents that interact according to a connected, undirected, communication graph and do not include feedback linearization of the agents' dynamics. Implementing the parallel control law on a testbed of fish robots required conducting system identification experiments to
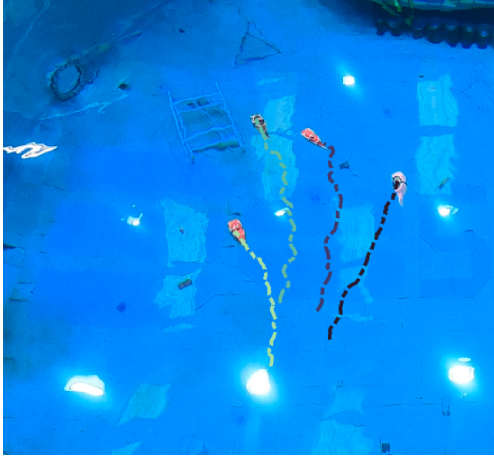
(a) Parallel formation control fish robot trajectory

(b) Parallel formation control fish robot trajectory with IMU erros

Figure 5.7: Parallel formation control of fish robot ground truth trajectory: (a) school of robotic fish swimming in a parallel formation. (b) errors affect the IMU of one fish causing to swim in a different direction than the rest of the school

characterize the motor dynamics and designing a torque tracking motor controller and estimator. Numerical simulations and experiments on a school of robotic fish demonstrate the proposed approach. In ongoing work, I seek to model the fluid interactions between fish robots and instrument the robotic fish with pressure sensors to exploit the hydrodynamic benefits of close-proximity swimming.

Chapter 6: Conclusion

Overall, this dissertation investigates bioinspired dynamic models of fish behavior in the areas of schooling, predation, and intermittent sensing and control. Although inspired by the behavior of aquatic species, this work can give insight to the behaviors of terrestrial and avian animals. These models not only enhance our understanding of the certain animal behaviors, but they also allow us to further study the benefits of these behaviors and apply then to autonomous robotic systems. This research was conducted using concepts from linear and nonlinear control theory, classical mechanics, differential game theory, and probability theory. Chapter 3 developed a hybrid model for intermittent dynamics to study the effects of non-overlapping sensing and control for a single agent and for multiple agents. Chapter 4 investigated pursuit interactions in a bounded environment. The predator changes its morphology to trap the prey, but doing so increases its hydrodynamic drag, and therefore its work to capture. This work devises a metric to determine the trade-off between minimizing the work to capture the prey and minimizing the prey's escape routes. Chapter 5 demonstrated the use of a nonlinear steering controller to drive a school of robotic fish into a parallel formation, developed an optimal sub-controller and estimator for torque tracking on a DC brushed motor.

6.1 Summary of Dissertation

This section summarizes the main results of this dissertation and suggest future research directions for these topics. First, I summarize the work presented in Chapter 3 and propose some ideas for future work in the intermittent sensing and control. Second, I summarize the work in Chapter 4 and present some of the many future directions this research can investigate. Third, I summarize Chapter 5.

6.1.1 Intermittent Locomotion with Non-overlapping Sensing and Control

Inspired by the intermittent swimming patterns where biological fish switch between active swimming and gliding through the water while desensitizing and sensitizing its sensory organs [7], I introduce a hybrid dynamic model that imitates this behavior and I explore the effects of non-overlapping sensing and control. To illustrate the effects of asynchronous sensing and control, I analyze the stability conditions of a closed-loop steering controller for a single particle and a heading synchronization controller for multiple particles.

The results from this work show that the stability conditions for the steering of a single particle and for the heading synchronization of multiple particles with synchronous burst phases using output feedback are the same, the these conditions depend on the additional features. Unlike the stability condition for a continuous closed-loop heading controller in Chapter 2, the stability conditions for this work depends on the strength of the actuation during the burst phase and the quality of the estimation during the coast phase. The strength of the actuation is defined as the product of the steering control gain and the

time duration for the burst phase. Similarly, the quality of the estimation is defined as the product of the linear observer gain and the time duration of the coast phase.

While exploring the limits of these stability conditions, I found that having weak actuations with high quality observations was exponentially stable. This result agreed with both our intuition and observations recorded in [3]. However, I also found that having very strong actuations with low quality observations was also exponentially stable. This result is surprising, and yet pretty astonishing, because it implies that large errors accumulated during the burst phase eventually go to zero as I encounter more coast phases.

The last two sections of Chapter 3 consider more realistic cases, where there are multiple particles with asynchronous burst phases. Building on the work in [22], I relaxed some assumptions and expanded there results to use an output feedback heading controller. The assumptions that I retained from [22] are the agents sure a fixed communication graph and all agents update on a uniform time horizon, i.e. share a homogeneous burst duration and overall cycle time. I relaxed the assumption that only non-connected agents can burst at the same time from [22], and allow a group of agents to have a synchronous burst phase. Regardless of the synchroneity of the burst phases, each of the particles have non-overlapping sensing and control.

With these assumptions, I derived a dynamic model for the entire ensemble of particles which generalizes to both the synchronous and asynchronous burst phase assumption. Analyzing the stability of the ensemble level dynamics proved that heading synchronization is locally exponentially stable and the conditions are identical to those in the single particle case.

For both the single particle and multiple particle cases, I evaluated local stability

conditions to synchronize the heading to a desired direction. The multi-particle case has three equilibrium points, i.e. synchronized, balanced, and parallel anti-parallel. When simulating the asynchronous multi-particle burst and coast model with initial conditions far from the synchronized equilibrium point, I noticed that the synchronization is still achieved. This observation may imply that the region of attraction of the asynchronous case may be larger than that of the synchronous.

The main idea with this burst and coast model is, since there is no sensing during the burst phase, I cannot apply feedback while bursting. However, future work in this area should explore the use of multiple sensory organs and develop a model where one or multiple senses get desensitized during the burst phase, but not all of them. This may be more realistic to what is observed in biological species. Also, future work should analyze the case of bounded actuator noise with bounded measurement noise in a single particle and compare these results to a continuously locomoting particle with the same actuator and measurement noise. This comparison will highlight the benefits or disadvantages of non-overlapping sensing and control for stochastic systems.

6.1.2   Bioinspired Pursuit in a Structured Environment

Pursuit has been a topic of interest to engineers, biologist, and military personnel, for over three centuries. Starting with the work from Pierre Bouguer in 1732 [92], scientist have created kinematic models of pursuit interactions to predict the behavior of adversaries and maximize there probability of capture. The work presented in Chapter 4 develops a pursuit interaction model inspired by observations of the predation between a

lionfish and its prey, and develops a metric used to determine the trade-off between mini-mizing the work to capture the prey and minimizing the prey's escape routes.

To study this trade-off, I modeled the dynamics of each agent, where the lionfish is modeled as a streamlined rigid body with symmetric appendages and constant speed in pure-pursuit of the prey, and the prey is modeled as a constant speed self-propelled particle that intermittently steers in a random flee direction to be less predictable to the lionfish. These behaviors are integrated in a differential game simulation where the prey wants to avoid capture from the predator and avoid collisions with the boundary, and the predator wants to capture the prey. The prey's random flee direction has a probability density function that depends on the prey's proximity to the boundary and the perceived width of the predator. The predator can chooses to expand its appendages to trap the prey, but doing so induces additional drag and increases its work to capture.

Devising a metric to determine when to prioritize minimizing work versus minimiz-ing escape routes was the greatest challenge of the work in this chapter, but I found that using the expected value of work as a function of predator's appendage orientation and the added drag due to appendage expansion was sufficient. The work to capture the prey depends on the predator's thrust and the time required to capture the prey given the kine-matics, but it does not account for the potential benefits of minimizing the possible maneu-vers of the prey. The expected work is computed using (2.12), where the probability density for the prey's heading is accounted for along with the work to capture. When the expected work for the appendages expanded is less than the expected work for the appendages re-tracted, the predator should prioritize trapping the prey. I call this the shape-changing condition.

By evaluating the shape-changing condition for a given prey location and all possible predator locations in the bounded environment, I determine the positions where the predator should prioritize trapping the prey. I call the outer boundary of this region the shape-changing boundary. The geometry of the shape-changing boundary depends on the prey's proximity to a structure. Studying the evolution of the shape-changing boundary, I qualitatively determined the existence of optimal pursuit trajectories for the predator that minimize the expected work.

Additional consideration must be made for the added hydrodynamic drag acting on the predator. Intuitively, one could understand that there is an upper limit for the amount of drag the predator can experience before it is never beneficial to expand its appendages. I compute this upper drag limit by solving the shape-changing condition for drag. While the angular geometry of the shape-changing boundary depends of the prey's proximity to a structure, the radial geometry depends on the added drag. As the added drag increases towards this upper limit, the max radial distance of the shape-changing boundary decreases.

While our model is useful in determining the trade off between minimizing work and minimizing escape routes, I guarantee that capture is achieved by making the predator faster than the prey. In reality, the prey's speed changes such that it is intermittently faster than the predator. Future work in this area should include and intermittently faster prey and find conditions on the relative speeds where capture is guaranteed.

Here we assume that the predator's appendages are always symmetric. This assumption resembles the behavior from observations [29], but perhaps symmetric appendages are the optimal expansion method. In ongoing and future work, I seek to control each appendage individually and optimize their orientation to further minimize the expected

97

work.

Lastly, the boundary can be used to aid the predator in capturing the prey, but real-world environments are more complex than a convex boundary. To enhance our understanding of the role that structures, i.e. coral reefs, trees, or boulders, play in pursuit interactions, future work should create virtual environments, devise parameters to characterize the density and convexity of the environment, and use a differential game to study how the pursuit interaction changes as a function of the environment.

6.1.3 Planar Formation Controller for a School of Robotic Fish

Inspired by the collective behavior found in many biological fish species, I demonstrate the utility of a novel nonlinear steering control law (5.9) that drives a school of robotic fish into a parallel formation. While the nonlinear steering control law was derived by other researchers, this dissertation experimentally validates its theoretical result by developing a robotic platform that implementing the control law.

The dynamics of the fish robot are modeled as the canonical Chaplygin sleigh model [54,77], where the actuator propelling and steering the system oscillates a reaction wheel at the sleigh's center of mass. The fish-inspired robots used in the experiments are each driven by a Pololu 12V DC motor (with a 4.4 to 1 gear ratio) that oscillates a reaction wheel located at each robot's center of mass. Each fish robot measures its orientation with an onboard BNO055 inertial measurement unit (IMU) sensor that features a built-in extended Kalman filter. A micro-SD card is used to store sensor data and a 900MHz xBee radio enables each fish robot to communicate with a ground station and other fish robots

on the water's surface. Each fish robot performs onboard sensor processing and control with a Teensy 3.2 microcontroller.

The nonlinear control (5.9) generates a reference torque that steers the fish robots to a parallel formation. However, on our robotic platform this torque cannot be commanded directly since the control input into the reaction wheel system is the voltage applied to the DC motor. Furthermore, the only available measurement is the angular velocity of the motor's shaft measured by an encoder. To track the reference torque a I implemented a linear-quadratic-Gaussian (LQG) controller and estimator as a low level controller.

System identification was performed on the DC motor using motor dynamics (5.11)−(5.14); after which the LQG low level controller and estimator were implemented. The performance of the low level controller and estimator was evaluated experimentally where I specified the heading of a single fish robot. A single was able to track a specified head and respond to a step input change in desired heading with a small average offset. This offset is likely due to the motor's deadband voltage region where the motor is unresponsive.

For the multi-fish robot experiment, I implemented the parallel formation controller (5.9) on four fish. The controller was able to align the average heading of each robot with a small offset of about twenty degrees. The motor's deadband region and excess gyro noise may have attributed to the magnitude of the offset.

To evaluating the performance of the controller on the robotic platform, I compute a polarization term, where the heading of each robot is compared to its neighbors headings, and plot it over time in Figure 5.6. This graph illustrates that at the start of six experiments the school's polarization term is high, heading are not aligned, and as the experiments progress the term decrease within some range. If the robots behaved as self-

propelled particles, as in [19, 20], then the polarization term would converge to the control gain K divided by the number of particles N. However, since the robots are required to oscillate their bodies to generate thrust for continued swimming, the polarization term also oscillates while converging to K_2/N.

While this successful demonstration of a nonlinear schooling controller is bioinspired, our implementation to align the fish robot's heading relied on the use of a XBee radio. Biological fish, of course use sensory organs like their eyes and their lateral line to sense neighboring fish and form schools. Future work in this area should seek to use an artificial lateral line system in conjunction with cameras to sense other robotic fish and swim in a parallel or circular formation.

Appendix A: Lyapunov's Direct and Indirect Methods

The behavior of an autonomous system near an equilibrium point can be characterized by using either Lyapunov's direct or indirect methods [93].

Lyapunov's direct method uses a scalar potential function candidate to determine the stability of an equilibrium point. Let $V(\boldsymbol{x})$ be a Lyapunov potential function candidate of the system $\dot{\boldsymbol{x}} = \boldsymbol{f}(\boldsymbol{x})$ such that $V(\boldsymbol{x}) > 0$ for all $\boldsymbol{x} \neq \boldsymbol{x}^*$, i.e., $V(\boldsymbol{x})$ is positive definite. The equilibrium point of a continuous-time system is asymptotically stable if $V(\boldsymbol{x})$ is continuously differentiable and $\dot{V}(\boldsymbol{x}) < 0$ for all $\boldsymbol{x} \neq \boldsymbol{x}^*$ [93], i.e., $\dot{V}(\boldsymbol{x})$ is negative definite. Similarly, in a discrete-time system where the dynamics are $\boldsymbol{x}(t+1) = \boldsymbol{f}(\boldsymbol{x}(t))$, an equilibrium point is asymptotically stable if there exist $V(\boldsymbol{x}(t)) > 0$ for all $\boldsymbol{x} \neq \boldsymbol{x}^*$ such that, $V(\boldsymbol{x}(t+1)) - V(\boldsymbol{x}(t)) < 0$ for all $\boldsymbol{x} \neq \boldsymbol{x}^*$.

Lyapunov's indirect method is used to determine the local stability of an equilibrium point. Let the dynamics of a system be $\dot{\boldsymbol{x}} = \boldsymbol{f}(\boldsymbol{x})$, where $\boldsymbol{x}$ is a vector of state variables. In Lyapunov's indirect method the system dynamics $\boldsymbol{f}(\boldsymbol{x})$ are linearized about an equilibrium point $\boldsymbol{x}^*$ to produce the Jacobian matrix

$$A = \frac{\partial \boldsymbol{f}}{\partial \boldsymbol{x}}\bigg|_{x=x^*}, \tag{A.1}$$

and the eigenvalues of (A.1) determines the behaviour of the equilibrium point. For a

linear continuous-time system, i.e., a flow, to have local exponential convergence to an equilibrium point, all eigenvalues must be in the left-half of the complex plane. Similarly, a discrete-time system, i.e., a map, has local exponential convergence to an equilibrium point if all eigenvalues are inside the unit circle of the complex plane [83].

For a one-dimensional linear map, the eigenvalue is the slope of the map at the equilibrium point. For a two-dimensional map, linearization requires the computation of the Jacobian matrix. The eigenvalues of this matrix can be calculated from its trace τ and determinant δ, i.e.,

$$\lambda_{1,2} = \frac{\tau \pm \sqrt{\tau^2 - 4\delta}}{2}. \tag{A.2}$$

Because $\lambda_{1,2}$ must be inside the unit circle, τ and δ must be inside the so-called stability triangle in the trace-determinant plane [83, p. 317]. The stability triangle is defined by the following three inequalities [83]:

$$
\begin{aligned}
\delta &< 1 \\
\delta &> -1 - \tau \\
\delta &> -1 + \tau.
\end{aligned}
\tag{A.3}
$$

Note, for a linear map, just like a linear flow, the strict inequalities in (A.3) can be replaced by non-strict inequalities.

Bibliography

[1] A. P. Soto and M. J. McHenry, "Pursuit predation with intermittent locomotion in zebrafish," *Journal of Experimental Biology*, vol. 223, no. 24, 2020.

[2] S. Bazazi, F. Bartumeus, J. J. Hale, and I. D. Couzin, "Intermittent motion in desert locusts: behavioural complexity in simple environments," *PLoS Comput Biol*, vol. 8, no. 5, p. e1002498, 2012.

[3] D. L. Kramer and R. L. McLaughlin, "The behavioral ecology of intermittent locomotion," *American Zoologist*, vol. 41, no. 2, pp. 137–153, 2001.

[4] E. J. Buskey, C. Coulter, and S. Strom, "Locomotory patterns of microzooplankton: potential effects on food selectivity of larval fish," *Bulletin of Marine Science*, vol. 53, no. 1, pp. 29–43, 1993.

[5] M. J. McHenry and G. V. Lauder, "The mechanical scaling of coasting in zebrafish (*Danio rerio*)," *J of Experimental Biology*, vol. 208, no. 12, pp. 2289–2301, 2005.

[6] A. McKee, A. P. Soto, P. Chen, and M. J. McHenry, "The sensory basis of schooling by intermittent swimming in the rummy-nose tetra (*Hemigrammus rhodostomus*)," *Proceedings of the Royal Society B*, vol. 287, no. 1937, p. 20200568, 2020.

[7] E. T. Lunsford, D. A. Skandalis, and J. C. Liao, "Efferent modulation of spontaneous lateral line activity during and after zebrafish motor commands," *J of Neurophysiology*, vol. 122, no. 6, pp. 2438–2448, 2019.

[8] K. E. Feitl, V. Ngo, and M. J. McHenry, "Are fish less responsive to a flow stimulus when swimming?" *J of Experimental Biology*, vol. 213, no. 18, pp. 3131–3137, 2010.

[9] I. M. Côté and A. Maljković, "Predation rates of Indo-Pacific lionfish on Bahamian coral reefs," *Marine Ecology Progress Series*, vol. 404, pp. 219–225, 2010.

[10] L. Tornabene and C. C. Baldwin, "A new mesophotic goby, *Palatogobius incendius* (Teleostei: Gobiidae), and the first record of invasive lionfish preying on undescribed biodiversity," *PloS one*, vol. 12, no. 5, p. e0177179, 2017.

[11] P. Paoletti and L. Mahadevan, "Intermittent locomotion as an optimal control strategy," *Proceedings of the Royal Society A: Mathematical, Physical and Engineering Sciences*, vol. 470, no. 2164, p. 20130535, 2014.

[12] L. Dai, G. He, X. Zhang, and X. Zhang, "Intermittent locomotion of a fish-like swimmer driven by passive elastic mechanism," *Bioinspiration & biomimetics*, vol. 13, no. 5, p. 056011, 2018.

[13] M. Chung, "On burst-and-coast swimming performance in fish-like locomotion," *Bioinspiration & biomimetics*, vol. 4, no. 3, p. 036001, 2009.

[14] T. Vicsek, A. Czirók, E. Ben-Jacob, I. Cohen, and O. Shochet, "Novel type of phase transition in a system of self-driven particles," *Physical review letters*, vol. 75, no. 6, p. 1226, 1995.

[15] A. Hu, J. H. Park, and M. Hu, "Consensus of nonlinear multiagent systems with intermittent dynamic event-triggered protocols," *Nonlinear Dynamics*, vol. 104, no. 2, pp. 1299–1313, 2021.

[16] Y. Gao and L. Wang, "Asynchronous consensus of continuous-time multi-agent systems with intermittent measurements," *International Journal of Control*, vol. 83, no. 3, pp. 552–562, 2010.

[17] F. Xiao and L. Wang, "Asynchronous consensus in continuous-time multi-agent systems with switching topology and time-varying delays," *IEEE Transactions on Automatic Control*, vol. 53, no. 8, pp. 1804–1816, 2008.

[18] W. Ren, R. W. Beard, and E. M. Atkins, "Information consensus in multivehicle cooperative control," *IEEE Control systems magazine*, vol. 27, no. 2, pp. 71–82, 2007.

[19] R. Sepulchre, D. A. Paley, and N. E. Leonard, "Stabilization of planar collective motion: All-to-all communication," *IEEE Transactions on Automatic Control*, vol. 52, no. 5, pp. 811–824, 2007.

[20] R. Sepulchre, D. Paley, and N. E. Leonard, "Stabilization of planar collective motion with limited communication," *IEEE Transactions on Automatic Control*, vol. 53, no. 3, pp. 706–719, 2008.

[21] L. Scardovi, A. Sarlette, and R. Sepulchre, "Synchronization and balancing on the N-torus," *Systems & Control Letters*, vol. 56, no. 5, pp. 335–341, 2007.

[22] A. Sarlette, R. Sepulchre, and N. E. Leonard, "Discrete-time synchronization on the n-torus," *Accepted for the 17th International Symposium on Mathematical Theory of Networks and Systems (Kyoto, Japan)*, 2006. [Online]. Available: http://www.montefiore.ulg.ac.be/services/stochastic/pubs/2006/SSL06

[23] A. A. Thompson, L. Cañuelas, and D. A. Paley, "Estimation and Control for Collective Motion with Intermittent Locomotion," in *2022 IEEE American Control Conference*. IEEE, 2022, pp. 747–754.

[24] S. Napora and D. A. Paley, "Observer-based feedback control for stabilization of collective motion," *IEEE Transactions on Control Systems Technology*, vol. 21, no. 5, pp. 1846–1857, 2012.

[25] M. A. Albins and P. J. Lyons, "Invasive red lionfish Pterois volitans blow directed jets of water at prey fish," *Marine Ecology Progress Series*, vol. 448, pp. 1–5, 2012.

[26] M. A. Albins and M. A. Hixon, "Worst case scenario: potential long-term effects of invasive predatory lionfish (Pterois volitans) on Atlantic and Caribbean coral-reef communities," *Environmental Biology of Fishes*, vol. 96, no. 10, pp. 1151–1157, 2013.

[27] S. J. Green, J. L. Akins, and I. M. Côté, "Foraging behaviour and prey consumption in the Indo-Pacific lionfish on Bahamian coral reefs," *Marine Ecology Progress Series*, vol. 433, pp. 159–167, 2011.

[28] A. N. Peterson, "The persistent-pursuit and evasion strategies of lionfish and their prey," Ph.D. dissertation, UC Irvine, 2022.

[29] A. N. Peterson and M. J. McHenry, "The persistent-predation strategy of the red lionfish (Pterois volitans)," *Proceedings of the Royal Society B: Biological Sciences*, vol. 289, no. 1980, p. 20221085, 2022.

[30] M. J. McHenry, J. L. Johansen, A. P. Soto, B. A. Free, D. A. Paley, and J. C. Liao, "The pursuit strategy of predatory bluefish (Pomatomus saltatrix)," *Proceedings of the Royal Society B*, vol. 286, no. 1897, p. 20182934, 2019.

[31] A. N. Peterson, A. P. Soto, and M. J. McHenry, "Pursuit and evasion strategies in the predator–prey interactions of fishes," *Integrative and comparative biology*, vol. 61, no. 2, pp. 668–680, 2021.

[32] D. Humphries and P. Driver, "Protean defence by prey animals," *Oecologia*, vol. 5, no. 4, pp. 285–302, 1970.

[33] A. Nair, K. Changsing, W. J. Stewart, and M. J. McHenry, "Fish prey change strategy with the direction of a threat," *Proceedings of the Royal Society B: Biological Sciences*, vol. 284, no. 1857, p. 20170393, 2017.

[34] A. Soto, W. J. Stewart, and M. J. McHenry, "When optimal strategy matters to prey fish," *Integrative and comparative biology*, vol. 55, no. 1, pp. 110–120, 2015.

[35] N. A. Shneydor, *Missile guidance and pursuit: kinematics, dynamics and control*. Elsevier, 1998, pp. 51–55.

[36] R. Isaacs, *Differential games: a mathematical theory with applications to warfare and pursuit, control and optimization*. Courier Corporation, 1999.

[37] Z. E. Fuchs, P. P. Khargonekar, and J. Evers, "Cooperative defense within a single-pursuer, two-evader pursuit evasion differential game," in *49th IEEE conference on decision and control (CDC)*. IEEE, 2010, pp. 3091–3097.

[38] W. Scott and N. E. Leonard, "Dynamics of pursuit and evasion in a heterogeneous herd," in *53rd IEEE Conference on Decision and Control*. IEEE, 2014, pp. 2920–2925.

[39] S. Pan, H. Huang, J. Ding, W. Zhang, C. J. Tomlin *et al.*, "Pursuit, evasion and defense in the plane," in *2012 American Control Conference (ACC)*. IEEE, 2012, pp. 4167–4173.

[40] E. Bakolas and P. Tsiotras, "Optimal pursuit of moving targets using dynamic Voronoi diagrams," in *49th IEEE conference on decision and control (CDC)*. IEEE, 2010, pp. 7431–7436.

[41] M. Dorothy, D. Maity, D. Shishika, and A. Von Moll, "One Apollonius circle is enough for many pursuit-evasion games," *arXiv preprint arXiv:2111.09205*, 2021.

[42] B. A. Free, M. J. McHenry, and D. A. Paley, "Probabilistic analytical modelling of predator–prey interactions in fishes," *Journal of the Royal Society Interface*, vol. 16, no. 150, p. 20180873, 2019.

[43] B. A. Free, J. Lee, and D. A. Paley, "Bioinspired pursuit with a swimming robot using feedback control of an internal rotor," *Bioinspiration & Biomimetics*, vol. 15, no. 3, p. 035005, 2020.

[44] S. Jin and Z. Qu, "Pursuit-evasion games with multi-pursuer vs. one fast evader," in *2010 8th World Congress on Intelligent Control and Automation*. IEEE, 2010, pp. 3184–3189.

[45] M. Ramana and M. Kothari, "A cooperative pursuit-evasion game of a high speed evader," in *2015 54th IEEE Conference on Decision and Control (CDC)*. IEEE, 2015, pp. 2969–2974.

[46] M. V. Ramana and M. Kothari, "Pursuit-evasion games of high speed evader," *Journal of intelligent & robotic systems*, vol. 85, no. 2, pp. 293–306, 2017.

[47] D. Weihs and P. W. Webb, "Optimal avoidance and evasion tactics in predator-prey interactions," *Journal of Theoretical Biology*, vol. 106, no. 2, pp. 189–206, 1984.

[48] T. Y. Moore, K. L. Cooper, A. A. Biewener, and R. Vasudevan, "Unpredictability of escape trajectory explains predator evasion ability and microhabitat preference of desert rodents," *Nature communications*, vol. 8, no. 1, pp. 1–9, 2017.

[49] W. Ren, R. W. Beard, and E. M. Atkins, "Information consensus in multivehicle cooperative control," *IEEE Control Systems Magazine*, vol. 27(2), no. 2, pp. 71–82, 2007.

[50] C. W. Reynolds, "Flocks, herds and schools: A distributed behavioral model," *Computer Graphics*, vol. 21(4), no. 4, pp. 25–34, 1987.

[51] T. Vicsek, A. Cziro'ok, E. Ben-Jacob, O. Cohen, and I. Shochet, "Novel type of phase transition in a system of self-driven particles," *Physical Review Letters*, vol. 75, no. 6, pp. 1226–1229, 1995.

[52] F. Zhang, P. Washington, and D. A. Paley, "A flexible, reaction-wheel-driven fish robot: Flow sensing and flow-relative control," in *American Control Conf.*, 2016, pp. 1221–1226.

[53] B. Free, M. K. Patnaik, and D. A. Paley, "Observability-based path-planning and flow-relative control of a bioinspired sensor array in a Karman vortex street," in *American Control Conf.*, 2017, pp. 548–554.

[54] J. Lee, B. Free, S. Santana, and D. A. Paley, "State-feedback control of an internal rotor for propelling and steering a flexible fish-inspired underwater vehicle," in *American Control Conf.*, 2019, pp. 2011–2016.

[55] F. Berlinger, M. Gauci, and R. Nagpal, "Implicit coordination for 3D underwater collective behaviors in a fish-inspired robot swarm," *Science Robotics*, vol. 6(50), no. 50, 2021.

[56] Z. Zhang, T. Yang, T. Zhang, F. Zhou, N. Cen, T. Li, and G. Xie, "Global vision-based formation control of soft robotic fish swarm," *Soft Robotics*, vol. 8(3), no. 3, pp. 310–318, 2021.

[57] Y. Cao, W. Yu, W. Ren, and G. Chen, "An overview of recent progress in the study of distributed multi-agent coordination," *IEEE Trans. Industrial Informatics*, vol. 9(1), no. 1, pp. 427–438, 2013.

[58] A. Olshevsky, "Linear time average consensus on fixed graphs," *IFAC-PapersOnLine*, vol. 48(22), no. 22, pp. 94–99, 2015.

[59] W. Ren and R. W. Beard, "Consensus seeking in multiagent systems under dynamically changing interaction topologies," *IEEE Trans. Automatic Control*, vol. 50(5), no. 5, pp. 655–661, 2005.

[60] Y. Cao and W. Ren, "Finite-time consensus for single-integrator kinematics with unknown inherent nonlinear dynamics under a directed interaction graph," in *American Control Conf.*, 2012, pp. 1603–1608.

[61] N. Chopra, "Output synchronization on strongly connected graphs," *IEEE Trans. Automatic Control*, vol. 57(11), no. 11, pp. 2896–2901, 2012.

[62] L. Moreau, "Stability of multiagent systems with time-dependent communication links," *IEEE Trans. Automatic Control*, vol. 50(2), no. 2, pp. 169–182, 2005.

[63] T. Li, M. Fu, L. Xie, and J.-F. Zhang, "Distributed consensus with limited communication data rate," *IEEE Trans. Automatic Control*, vol. 56(2), no. 2, pp. 279–292, 2011.

[64] R. A. Horn and C. R. Johnson, *Matrix Analysis*. New York, NY: Cambridge University Press, 1990.

[65] Y. Zhang and Y.-P. Tian, "Consentability and protocol design of multi-agent systems with stochastic switching topology," *Automatica*, vol. 45(5), no. 5, pp. 1195–1201, 2009.

[66] W. Yu, G. Chen, M. Cao, and J. Kurths, "Second-order consensus for multiagent systems with directed topologies and nonlinear dynamics," *IEEE Trans. Systems, Man, and Cybernetics, Part B (Cybernetics)*, vol. 40(3), no. 3, pp. 881–891, 2010.

[67] D. A. Paley, "Stabilization of collective motion on a sphere," *Automatica*, vol. 45(1), no. 1, pp. 212–216, 2009.

[68] E. W. Justh and P. Krishnaprasad, "Equilibria and steering laws for planar formations," *Systems & Control letters*, vol. 52, no. 1, pp. 25–38, 2004.

[69] S. Napora and D. A. Paley, "Observer-based feedback control for stabilization of collective motion," *IEEE Trans. Control Systems Technology*, vol. 21(5), no. 5, pp. 1846–1857, 2013.

[70] D. A. Paley, "Cooperative control of an autonomous sampling network in an external flow field," in *IEEE Conf. Decision and Control*. IEEE, 2008, pp. 3095–3100.

[71] A. Jain and D. Ghose, "Trajectory-constrained collective circular motion with different phase arrangements," *IEEE Trans. Automatic Control*, vol. 65(5), no. 5, pp. 1–8, 2019.

[72] L. Brinón-Arranz, A. Seuret, and C. Canudas-de Wit, "Cooperative control design for time-varying formations of multi-agent systems," *IEEE Trans. Automatic Control*, vol. 59(8), no. 8, pp. 2283–2288, 2014.

[73] X. Yu and L. Liu, "Cooperative control for moving-target circular formation of nonholonomic vehicles," *IEEE Trans. Automatic Control*, vol. 62(7), no. 7, pp. 3448–3454, 2017.

[74] X. Yu, L. Liu, and G. Feng, "Distributed circular formation control of nonholonomic vehicles without direct distance measurements," *IEEE Trans. Automatic Control*, vol. 63(8), no. 8, pp. 2730–2737, 2018.

[75] D. A. Paley, A. A. Thompson, A. Wolek, and P. Ghanem, "Planar formation control of a school of robotic fish: Theory and experiments," *Frontiers in Control Engineering*, p. 15, 2021.

[76] A. A. Thompson, A. N. Peterson, M. J. McHenry, and D. A. Paley, "A lionfish-inspired predation strategy in planar structured environments," *Bioinspiration & Biomimetics*, 2023.

[77] P. Ghanem, A. Wolek, and D. A. Paley, "Planar formation control of a school of robotic fish," in *2020 American Control Conference*. IEEE, 2020, pp. 1653–1658.

[78] L.-s. Hahn, *Complex numbers and geometry*. Cambridge University Press, 1994, vol. 1, pp. 24–25.

[79] M. Mesbahi and M. Egerstedt, *Graph theoretic methods in multiagent networks*. Princeton University Press, 2010.

[80] J. A. Acebrón, L. L. Bonilla, C. J. P. Vicente, F. Ritort, and R. Spigler, "The Kuramoto model: A simple paradigm for synchronization phenomena," *Reviews of Modern Physics*, vol. 77, no. 1, p. 137, 2005.

[81] N. J. Kasdin and D. A. Paley, *Engineering Dynamics*. Princeton University Press, 2011, pp. 148–150.

[82] R. G. Brown and P. Y. Hwang, *Introduction to Random Signals and Applied Kalman Filtering: with MATLAB Exercises and Solutions*. John Wiley & Sons, 1997.

[83] G.-I. Bischi, C. Chiarella, M. Kopel, F. Szidarovszky *et al.*, *Nonlinear oligopolies*. Springer, 2010.

[84] R. Ruiz-Carus, R. E. Matheson Jr, D. E. Roberts Jr, and P. E. Whitfield, "The western pacific red lionfish, *Pterois volitans (Scorpaenidae)*, in florida: evidence for reproduction and parasitism in the first exotic marine fish established in state waters," *Biological Conservation*, vol. 128, no. 3, pp. 384–390, 2006.

[85] S. D. Kelly, M. J. Fairchild, P. M. Hassing, and P. Tallapragada, "Proportional heading control for planar navigation: The Chaplygin beanie and fishlike robotic swimming," in *American Control Conf.*, 2012, pp. 4885–4890.

[86] D. A. Paley, "Cooperative Control of Collective Motion for Ocean Sampling with Autonomous Vehicles," Ph.D. dissertation, Princeton University, 2007.

[87] A. M. Bloch, "The Chaplygin Sleigh," in *Nonholonomic Mechanics and Control*. New York, NY: Springer, 2003, pp. 25–29.

[88] B. Pollard, V. Fedonyuk, and P. Tallapragada, "Swimming on limit cycles with nonholonomic constraints," *Nonlinear Dynamics*, vol. 97(4), no. 4, pp. 2453–2468, 2019.

[89] I. The MathWorks, "Track a face in scene," 2019. [Online]. Available: https://www.mathworks.com/help/vision/ug/track-a-face.html

[90] S.-H. Kim, *Electric Motor Control: DC, AC, and BLDC motors*. Elsevier, 2017.

[91] J. L. Crassidis and J. L. Junkins, *Optimal Estimation of Dynamic Systems*. CRC press, 2011.

[92] S. Tabachnikov, "Chases and escapes. the mathematics of pursuit and evasion by paul j. nahin: Princeton: Princeton university press, 2007, 253 pp." *The Mathematical Intelligencer*, vol. 31, pp. 7–40, 2009.

[93] H. K. Khalil and J. W. Grizzle, *Nonlinear systems*. Prentice hall Upper Saddle River, NJ, 2002, vol. 3.